



Contents lists available at ScienceDirect

Tunnelling and Underground Space Technology

journal homepage: www.elsevier.com/locate/tust

The application of distinct lattice spring model to zonal disintegration within deep rock masses

Jianjun Ma^a, Peijie Yin^b, Linchong Huang^{c,*}, Yu Liang^c^a School of Civil Engineering, Sun Yat-Sen University, Guangzhou 510006, China^b School of Highway, Chang'an University, Xi'an 710000, China^c School of Aeronautics and Astronautics, Sun Yat-Sen University, Guangzhou 510006, China

ARTICLE INFO

Keywords:

DLSM
Zonal disintegration
Rock masses
Heterogeneity
Weibull distribution

ABSTRACT

Zonal disintegration has been frequently encountered in many tunnelling projects such as deep mining and water tunnels in hydropower stations. The mechanisms of this phenomenon cannot be explained reasonably through conventional mesh-based numerical approaches. Thus, in this study, a dual coupled Micro-Macro Continuum-Discontinuum approach named as Distinct Lattice Spring Model (DLSM) has been applied to investigate the mechanisms of zonal disintegration within deep rock masses. Firstly, the 3D numerical modes are built up, with fixed boundaries being set for far fields and displacement loading being applied along the tunnel axis. This numerical mode is then validated through comparing model simulation with laboratory model tests, where reasonable agreement has been achieved for all cases considered (normal rock mass and layered rock mass with different joint spaces). To cater for real tunnels within various rock masses, tunnels excavated in deep rock masses with different sizes, shapes and material heterogeneities are investigated. Numerical study demonstrates that, the DLSM is capable to reproduce the process of zonal disintegration explicitly, along with which the mechanical responses have been captured reasonably. It shows that, the occurrence of zonal disintegration mainly depends on the material heterogeneities and the in-situ stress level. The fracture patterns formed during zonal disintegration rely on tunnels' shape, size and the distribution of local weakness in surrounding rock masses.

1. Introduction

Zonal disintegration has been drawing increasing attentions in geotechnical and mining engineering owing to the rapid development of high-speed railways, high ways, hydropower stations and deep mines (Chen et al., 2017; Jia and Zhu, 2015; Zhang et al., 2017; Zuo et al., 2012). This phenomenon is characterised by the alternate occurrence of fractured zone and non-fractured zone in rock masses around the vicinity of excavated tunnels (Adams and Jager, 1980; Shemyakin et al., 1986b; Zhou and Shou, 2013; Zuo et al., 2012). Also, it can be only observed during the excavation of tunnels in deep rock masses, with extensive evidences being reported from the excavation in deep mines (Adams and Jager, 1980; Borzykh, 1990; Shemyakin et al., 1986b; Zuo et al., 2012), constructions in hydropower stations (Lin et al., 2015; 2013; Qian et al., 2009), and high speed railways (She and Lin, 2014) in mountain-valley areas. As common support methods for shallow excavations may not be suitable for deep working space with zonal disintegration thus, a better understanding on zonal disintegration plays a

significant role in excavation and support designs for cavities in deep rock masses.

Generally, deep rock masses are characterised by high in-situ stress level and high stiffness. Due to the difficulty in conducting experimental work in deep rock masses, extensive studies on the mechanisms of zonal disintegration have been carried out in terms of in-situ observation, physical model tests, theoretical analysis, and numerical investigation. Notable work published in in-situ observation includes the filed monitoring analysis of Doornfontein Gold Mine by Adams and Jager (1980), the experimental observations in the mines of Talnakh-Oktyarb' skiy deposit by Shemyakin et al. (1986b), and other deep excavations (Borzykh, 1990; Li et al., 2008; She and Lin, 2014). These observations demonstrate that zonal disintegration occurs at deep rock masses under a certain condition, where the maximum principle stress is the horizontal stress along the tunnel axis other than the vertical stress or the horizontal stress perpendicular to the tunnel axis (Jia et al., 2014; Li et al., 2008). Similar view also has been pointed out after studying some physical model tests on equivalent materials conducted

* Corresponding author.

E-mail address: hlinch@mail.sysu.edu.cn (L. Huang).<https://doi.org/10.1016/j.tust.2019.04.017>

Received 30 September 2018; Received in revised form 13 February 2019; Accepted 15 April 2019

Available online 03 May 2019

0886-7798/ © 2019 Elsevier Ltd. All rights reserved.

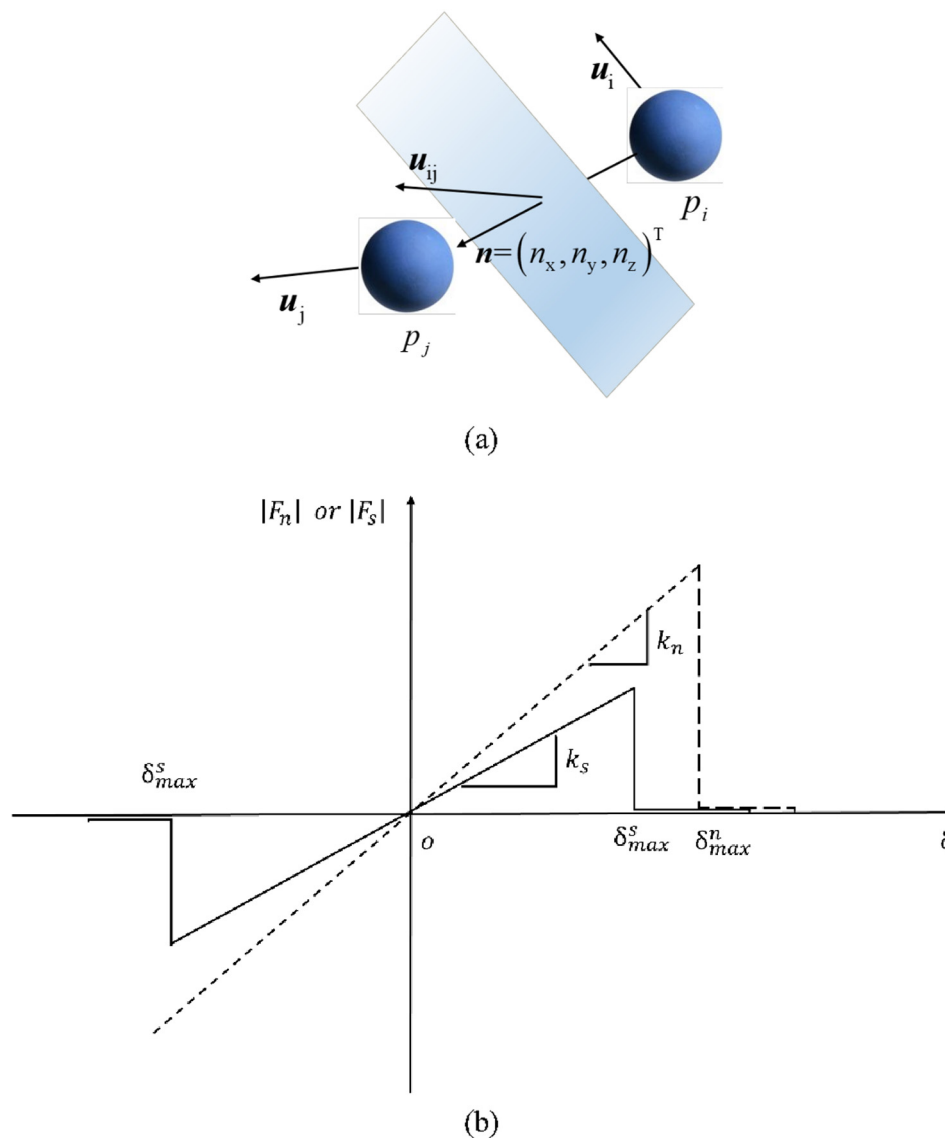


Fig. 1. Graphical description of DSLM, (a) the relative displacement between two linked ball elements, and (b) constitutive laws of lattice springs (Zhao et al. 2011).

in laboratory (Chen et al., 2017; Gu et al., 2008; Sellers and Klerck, 2000; Shemyakin et al., 1986a; Zhang et al., 2017). Based on the filed observations and laboratory physical model tests, some theoretical analysis have been presented (Guzev and Paroshin, 2001; Reva, 2002; Shemyakin et al., 1987; Zhou et al., 2008). However, these studies focus on zonal disintegration phenomenon and the characteristics of fracture patterns, with no detailed explanations being given to the mechanisms and occurrence conditions of zonal disintegration (Zuo et al., 2012). It seems that, these filed observations, laboratory model tests and theoretical analysis cannot provide a clear view of how zonal disintegration occurs and how its corresponding fracture rings form. Thus, numerical simulation would be an alternative to study the mechanisms of zonal disintegration.

Numerical investigation presented in this field are mainly achieved by the classical mesh-based numerical methods, i.e., RFPA^{3D} models (Jia et al., 2012; Jia and Zhu, 2015; Zuo et al., 2012), ELFEN (Sellers and Klerck, 2000), AUTODYN (Zhu et al., 2014), Weak-element model (Qian et al., 2009), non-Euclidean continuum models (Guzev and Paroshin, 2001; Zhou and Shou, 2013), Abacus (Zhang et al., 2017) and FLAC^{3D} models (Jia et al., 2014; Li et al., 2013; Zhang et al., 2012). Although these numerical models captured some fundamental characteristics of zonal disintegration, the mechanisms and occurrence

conditions of zonal disintegration are still debatable. For example, Zhu et al. (2014) applied dynamic load (P-wave) to a deep excavation, and concluded that the dynamic approach other than static mechanics could better explain the phenomenon of zonal disintegration, which is against most numerical studies based on static mechanics mentioned above (Weak-element, ELFEN, RFPA, FLAC models). In the approach of static mechanics, Zhou et al. (2008) believed that zonal disintegration occurs when the in-situ stress exceeds the uniaxial compression strength of rock masses. While, Li et al. (2013) supposed that the alternate occurrence of fracture zone also depends on the excavation time, similar conclusion also could be found in the work of (Zhou and Shou, 2013; Zuo et al., 2012). Other researchers focused on the occurrence conditions of zonal disintegration from the perspectives of: tri-axial/bi-axial stress ratio (Jia et al., 2012; Qian et al., 2009), the direction of maximum principle stress (Gu et al., 2008; Zuo et al., 2012); rock masses' heterogeneity level (Jia and Zhu, 2015; Sellers and Klerck, 2000).

Although the above contributions provide valuable insights into the mechanisms of zonal disintegration, a general conclusion has not been reached. In real deep tunnelling/mining engineering, the size of underground openings and their shapes may vary from site to site. Yet, these factors have not been considered in previous investigations. Particularly, the fracture patterns and failure process have not been

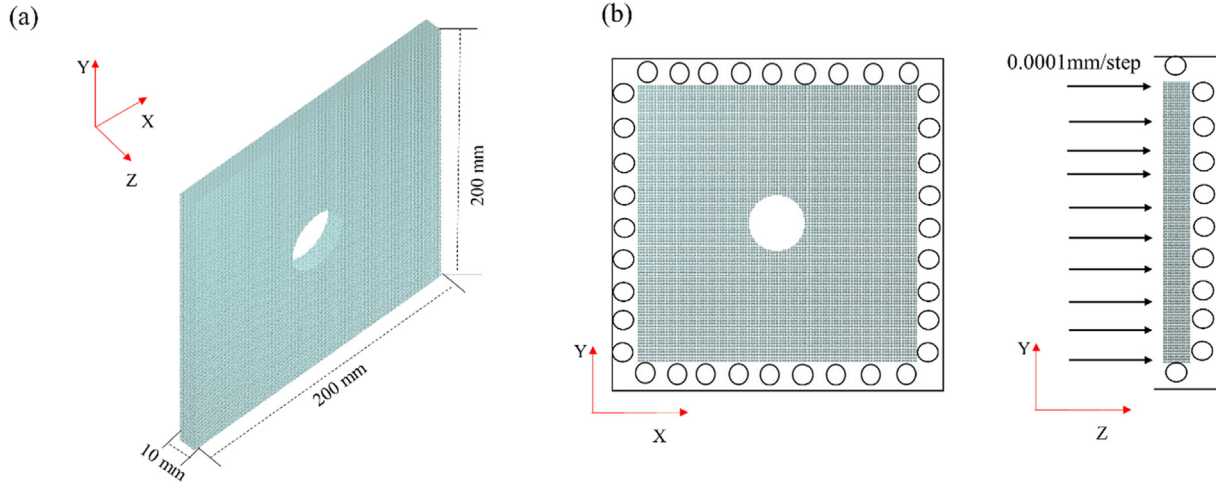


Fig. 2. Numerical model and boundary conditions, (a) size of numerical domain; and (b) boundary conditions.

well presented explicitly through conventional mesh-based numerical models. The main objective of this paper is to obtain a fundamental understanding of the mechanisms and occurrence conditions of zonal disintegration. Specifically, 3D numerical models are built up through a Distinct Lattice Spring Model (DLSM) proposed by Zhao et al. (2011). DLSM has been proved to be an appropriate tool to simulate the process of particle breakage of rock masses with irregular shapes and various heterogeneity levels in previous research (Ma and Zhao, 2015). To cater for real tunnels within various rock masses, tunnels excavated in deep rock masses with different sizes, shapes and material heterogeneities are investigated.

2. Validation of DLSM

2.1. Distinct lattice spring model

Distinct lattice spring model (DLSM) is a dual coupled Micro-Macro Continuum-Discontinuum numerical model proposed by Zhao et al. (2011). The unit elements adopted in DLSM are rigid particle balls, through the interactions of which the mechanical behaviours of rock masses can be captured. In DLSM, the connection bond between adjacent balls is composed of a normal and shear springs, which enable DLSM to model the multi-body force by evaluating the spring deformation from the local strain rather than the particle displacement. As shown in Fig. 1(a), the relative displacement (\mathbf{u}_{ij}) of two linked adjacent ball elements (p_i and p_j) is expressed as (Zhao et al., 2011)

$$\mathbf{u}_{ij} = \mathbf{u}_j - \mathbf{u}_i \quad (1)$$

with the normal unit vector $\mathbf{n} = (n_x, n_y, n_z)^T$ defining the direction from p_i to p_j , the normal and shear displacements thus can be calculated as (Zhao et al., 2011)

$$\begin{aligned} \mathbf{u}_{ij}^n &= (\mathbf{u}_{ij} \cdot \mathbf{n})\mathbf{n} \\ \mathbf{u}_{ij}^s &= \mathbf{u}_{ij} - \mathbf{u}_{ij}^n \end{aligned} \quad (2)$$

The embodied constitutive laws applied for two kinds of springs are quiet simple and stable, as shown in Fig. 1(b). Two springs follow the linear elastic law whenever the normal (u^n) or shear displacement (u^s) of the bond is smaller than the given threshold values (δ_n^{\max} for normal spring and δ_s^{\max} for shear spring). Otherwise, the bond is broken, and it becomes a contact bond with zero strength being applied to a normal spring. Thus, avoiding violating the rotational invariance, this constitutive law enables DLSM to represent the diversity of Poisson's ratio for various rock materials. The coupling effects between microscopic spring parameters (k_n and k_s) and macroscopic material constants are achieved through the Cauchy-Born rules and the hyperelasticity theory.

Common material parameters such as Young's modulus (E) and Poisson's ratio (ν), and homogeneous index parameter m (for heterogeneous materials) are required for model simulation (Zhao et al., 2011). Thus, DLSM can directly use macroscopic parameters and adopt general lattice structures to capture the mechanical behaviours of a variety of rock materials. For a better demonstration of material's damage, broken ratio is introduced in DLSM to define the portion of elements, the connected bonds of which have been broken. More details regarding to the development and application of DLSM can be referred to references (Zhao, 2017; Zhao et al., 2013; 2011; Zhao and Zhao, 2012).

The heterogeneity of material models in this study is described by Weibull distribution, which assumes that the strength parameters (failure strength σ_c and Young's modulus E_c) of each ball element follow a random distribution as expressed by,

$$\psi(\sigma) = \frac{m}{\sigma_0} \left(\frac{\sigma}{\sigma_0}\right)^{m-1} \exp\left(-\left(\frac{\sigma}{\sigma_0}\right)^m\right) \quad (3)$$

in which σ is the element strength parameter; σ_0 is the average value of the strength parameter (average compressive strength σ_0 and elastic modulus E_0). The homogeneous index parameter m controls the shapes of density function and is the indicator of material homogeneity. Note that, a larger value of m indicates a more homogeneous material and vice versa (Tang, 1997). Previous research demonstrates that the value of m range from 1.5 to 10, implying rock materials from relative heterogeneity to relative homogeneity (Tang et al., 2000). Thus, this study follow this suggestion to define the values of m to account for the heterogeneity of rock masses: $m = 2$ and $m = 5$; $m = \text{infinity}$ for homogeneous material, which is also named as H for a material reference.

2.2. Numerical model

DLSM validation is achieved through studying a 3D geotechnical model test carried out by Zhang et al. (2017). The laboratory model was precast, using similar materials in terms of physical and mechanical parameters for Dingji Coal Mine, where the mass ratio of iron powder, barite powder and quartz sand was set as 1:1.2:0.38. The side length of this precast cubic model is 600 mm, a circular tunnel with inner diameter of 100 mm was excavated. The maximum principle stress was applied along the tunnel axis. The numerical model developed by DLSM is shown in Fig. 2(a). The spatial dimension of the investigated rock mass is 200 mm(width) X 200 mm(height) X 10 mm (depth), with a total number of ball elements being around 400,000. A circular tunnel with radius of 10 mm is excavated in the center of this rock mass. Considering that zonal disintegration occurs in deep rock masses where the

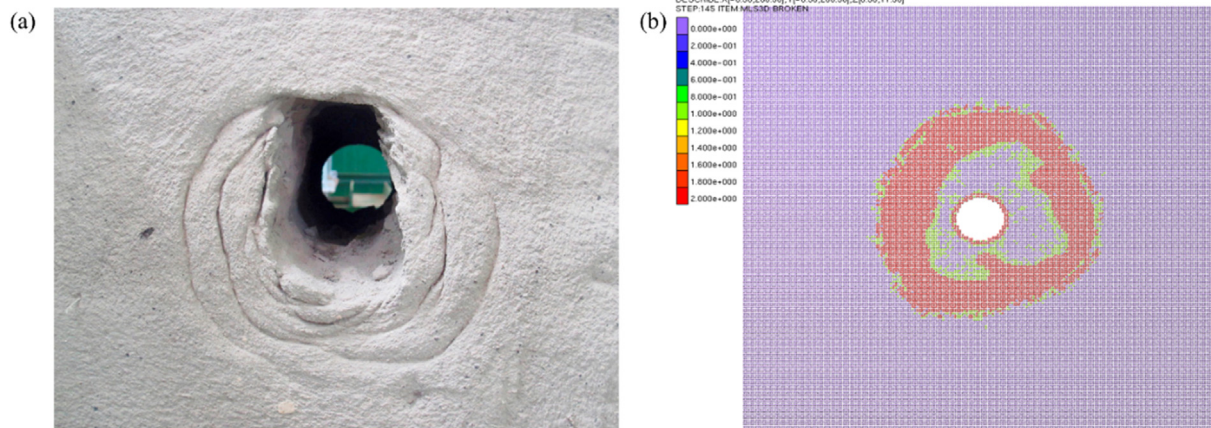


Fig. 3. Comparison of fracture patterns: (a) laboratory model test (Zhang et al. 2017), and (b) numerical simulation. For broken fields, legend values range from 0–2, colours fall into the range of purple-to-red. Purple = 0, represents elements with intact or unbroken contact bonds; Green = 1, represents elements with contact broken bonds (compressed zone); and Red = 2, represents elements with un-contact bonds or tension fracture mode (same legend for the rest). (For interpretation of the references to colour in this figure legend, the reader is referred to the web version of this article.)

maximum principle stress is parallel with tunnel axis (Gu et al., 2008; Jia et al., 2014; Li et al., 2008; Shemyakin et al., 1986b; Zhang et al., 2017), a constant displacement load along the tunnel axis (1.0×10^{-4} mm/step) is applied, and boundaries parallel to the bottom, top, left, right and back faces are fixed in their normal direction (Fig. 2(b)).

The material parameters employed here are: $E = 32$ GPa and $\nu = 0.25$ for a rock mass, $m = 2$ for the consideration of heterogeneity. $d = 0.5$ mm is the diameter of individual ball element/particle, and $D_p = 0.25$ is the damping ratio for steady-state condition (Zhao et al., 2011; Zhao, 2017).

2.3. Comparison between model simulation and laboratory test

2.3.1. DSLM validation for normal rock mass without joints

The final fracture patterns of both laboratory model test and numerical simulation are depicted in Fig. 3. The resulting fracture zones are demonstrated explicitly with broken fields (Fig. 3(b)) by numerical simulation. For a better demonstration of fracture zones in DSLM, two kinds of connection states are defined for damaged/broken elements. One is the contact state (green colour in Fig. 3(b)) for elements being connected by a bond with zero strength, and the other is the un-contact state or tension cracking state (red colour in Fig. 3(b)) for elements being disconnected due to a larger displacement of ball elements. Compared with laboratory model test, an irregular intact zone has been observed between the first compression zone and the first appeared fracture zone beside the tunnel wall. Thus, five irregular zones appear alternately from the tunnel wall to its far field, the first slim fracture zone, intact zone, compression zone, the main fracture zone and the slim compression zone on the border of the outer intact zone.

The main characteristics of alternately appeared fracture patterns and compression fields are similar to that of laboratory mode test (Fig. 3(a)). The main discrepancies between model test and numerical simulation are the sizes and numbers of fracture rings, as can be seen in Fig. 3(a). The model test produced 3 narrow fracture zones to separate intact zones, while numerical model reproduces two main wider fracture zones (including 2 narrow compressive zones and 2 large tension zones) with irregular shapes. The main discrepancy may be attributed to the difference of grain size applied in both study (Zhao et al., 2011; 2013; Zhao, 2017). The laboratory model was precast by iron powder, barite powder and quartz sand, the sizes of which (averagely $d = 0.13$ mm, compared with side length of 600 mm) are much smaller than the size of ball element in DSLM ($d = 0.5$ mm, compared with side length of 200 mm). In addition, the final fracture patterns and the

propagation of both tension fracturing zones and compression fields vary upon the variation of heterogeneities, as fracture zones propagate locally with the preference of weak parts of rock masses (Ma and Zhao, 2015). Thus, applying the displacement loading along the longitudinal axis of a tunnel would reproduce zonal disintegration in normal rock mass without joints.

For a better comparison between numerical results and model tests, normalized radial displacements (radial displacement along horizontal direction U_x over tunnel radiate r_0) versus normalized axial distance from tunnel centre (r/r_0) are plotted in Fig. 4. It is apparent that, the radial displacement curve in both study are characterized by alternative appearance of wave crest and trough, corresponding to zonal disintegration of surrounding rock mass. The largest displacement appears at the vicinity of tunnel wall, where the surrounding rock mass is destroyed completed and can be regarded as a traditional damage zone in shallow buried tunnel (Zhang et al., 2017). Due to the larger grain size in DSLM model, fracture zones are featured with larger size in this study, corresponding to larger distance between wave peaks along radial distance. For a better understanding of model performance, displacement curves at different loading steps are plotted in Fig. 4(b) as well. It is found that, some former formed tension fractures tend to close with increasing loading, which can justify the closure of fractures in some mining projects. This also can be confirmed by the compression damage zones depicted in Fig. 3(b).

Fig. 5 shows the stresses versus displacement along tunnel axial produced by numerical modelling. Obviously, the mechanical response of this rock mass are relatively elastic brittle, as the stress-displacement curves are almost linear until reaching the peak, beyond which the stresses drop quickly to residual state with almost no strength in the rock mass. The axial stress-displacement curve reaches to their peak strength points, corresponding to the final patterns of zonal disintegration. While, the lateral peak compression stresses appear later than their corresponding axial peak compression stresses, which shows some time lag effects on two principle stresses. Thus, essential support should be activated before the peak stress points for the consideration of tunnel's safety.

For the analysis of occurrence condition of zonal disintegration, stress ratios (σ_z/σ_x , σ_y/σ_x) versus axial displacement are plotted together in Fig. 6. It suggests that zonal disintegration occurs when the axial stress along tunnel is around 2–3 times the lateral stress, which agrees well with some filed observation and model tests (Chen et al., 2017; Gu et al., 2008; Jia and Zhu, 2015; Shemyakin et al., 1986b; Zhang et al., 2017). Therefore, the zonal disintegration could be captured by DSLM model with reasonable accuracy.

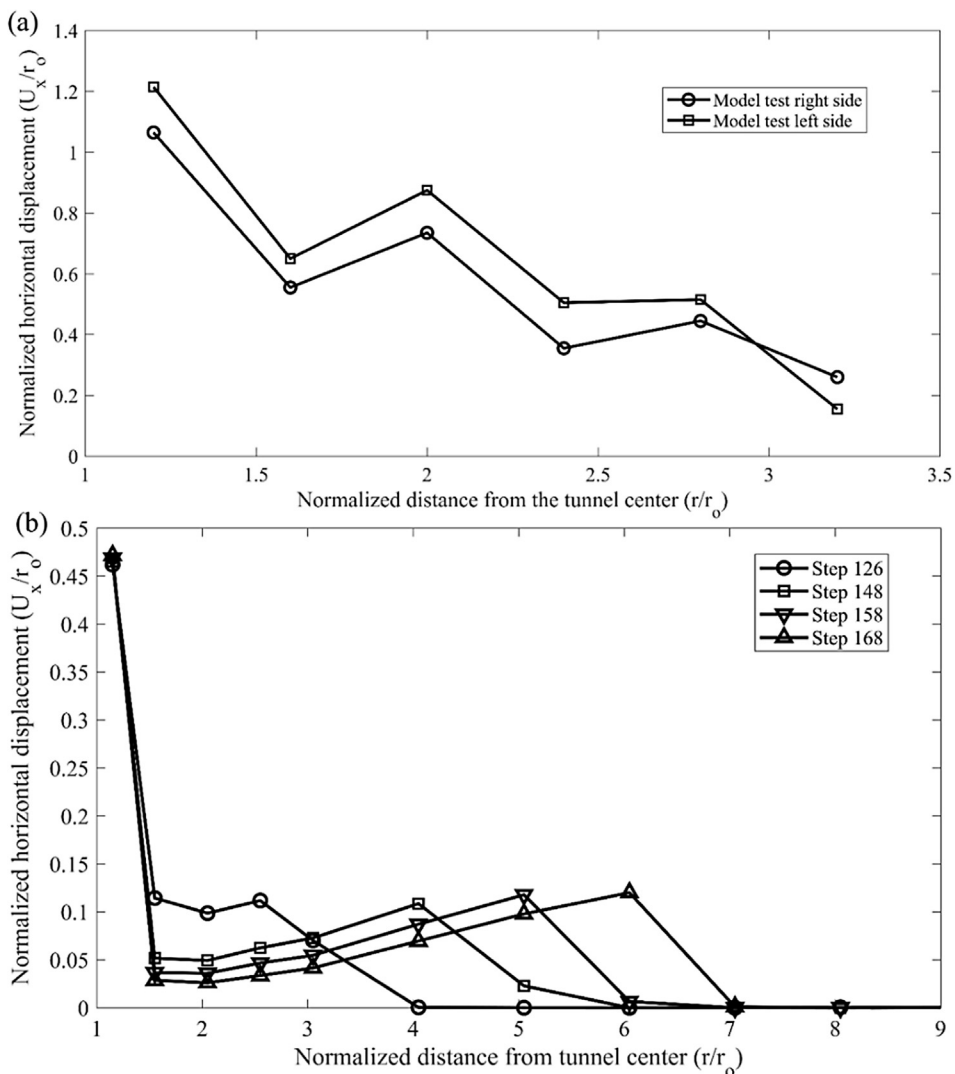


Fig. 4. Comparison of normalized horizontal displacement: (a) laboratory model testing result on the final loading step (Zhang et al. 2017), and (b) numerical results at 4 loading steps.

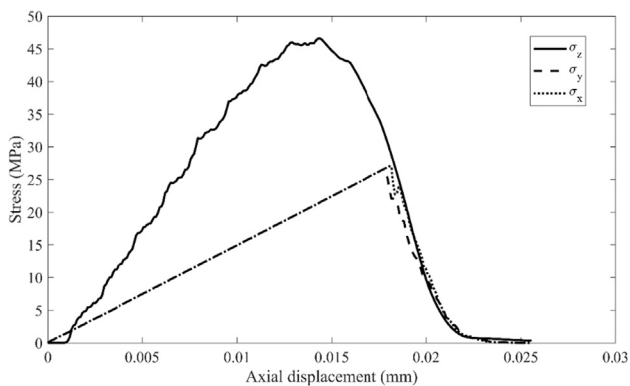


Fig. 5. Stresses versus displacement along tunnel axial (DLSM results).

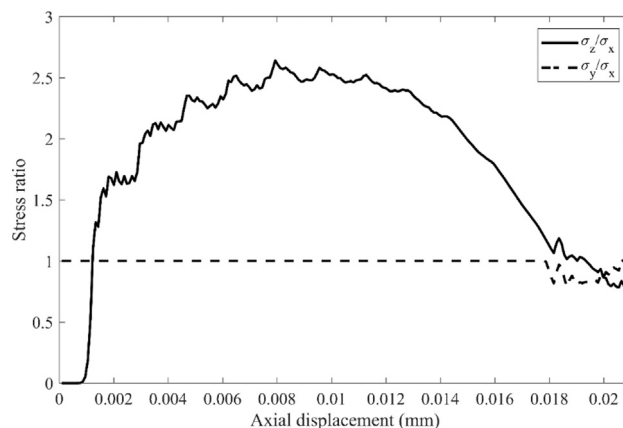


Fig. 6. Stress ratio versus tunnel axial displacement.

2.3.2. DSLM validation for jointed rock mass

For a better demonstration of DSLM validation, zonal disintegration simulation on layered rock mass with different joint spaces (joint space = r_0 and $2r_0$) have been carried out in this section. Note that, these weak joints are modelled by virtual joint plane method in DSLM, which has been proved as an effective approach to treat discontinuous elements in DEM (Zhao et al., 2011). The numerical modes, final

fracture patterns produced by DSLM and experimental model tests are compared in Fig. 7. In both two cases, three main fracture zones are reproduced alternatively by DSLM, enclosing one major irregular intact zone and some discontinuous sub-intact zones. Compared with laboratory model tests (Zhang et al., 2014), the main characteristics of fracture patterns in two cases match with experimental results

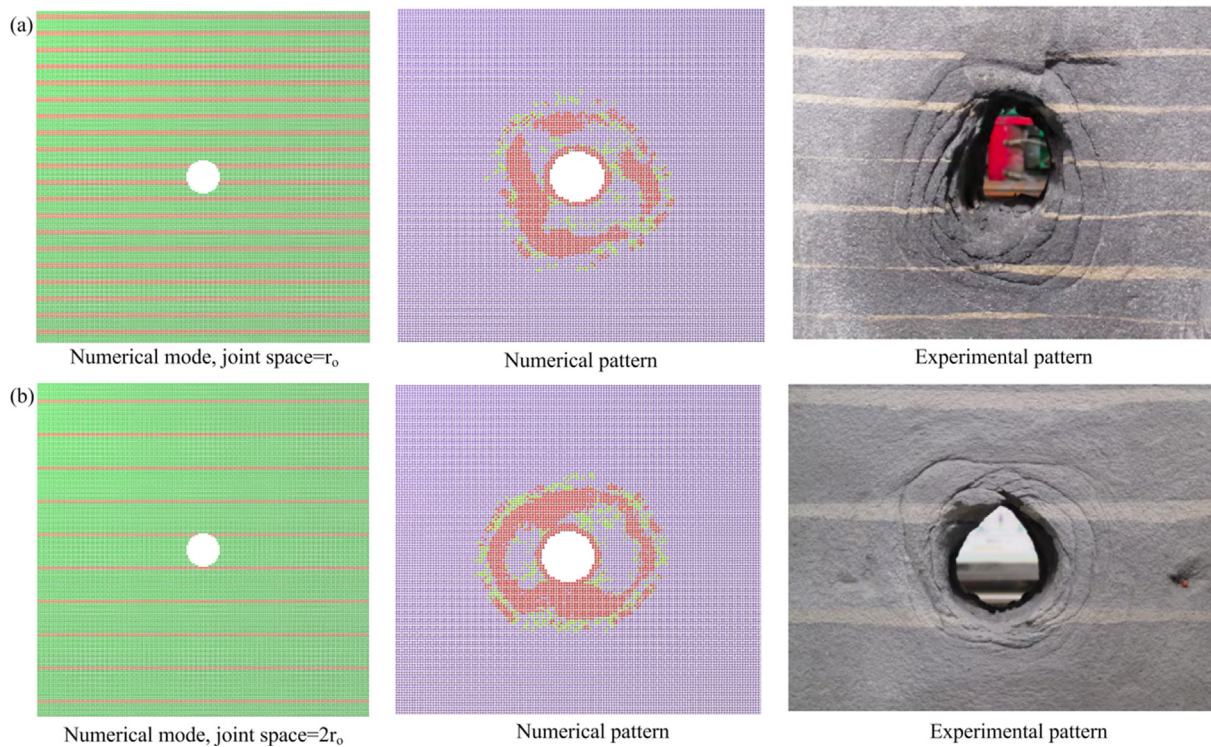


Fig. 7. Comparison of fracture patterns from numerical simulation and laboratory model tests (Zhang et al. 2017), (a) joint space = r_o , and (b) joint space = $2r_o$.

reasonably. Owing to the existence of layered weak joints, the main irregular intact zone between two main fracture zones is more tortuous compared with that of the normal rock mass (in Section 2.3.1), which has been confirmed by experimental model tests. In addition, numerical simulation also indicates that, layered joints would not affect the occurrence of zonal disintegration. However, joint spaces impose important impact on the final fracture patterns in two cases, as both numerical simulation and experimental model tests confirm that the rock mass with smaller joint space is characterized by narrow fracture zones and larger disintegration range.

For a better demonstration of the capacity of DLSSM, normalized radial strain (ϵ_r/r_o) versus normalized distance from tunnel centre (r/r_o) are plotted in Fig. 8. Obviously, the radial strain curve in both numerical simulation and model tests (Zhang et al., 2014) are characterized by alternative appearance of wave crest and trough, which correspond to fractured zones and intact zones. Three main irregular fracture patterns have been reproduced by both numerical simulation and experimental model tests, thus indicating DLSSM is capable to reproduce zonal disintegration phenomenon in rock mass with layered joints. The effects of joint space also have been demonstrated explicitly by DLSSM simulation, where the larger radial strains have been observed in rock mass with small joint space. This also confirms that, DLSSM results match with model experimental results reasonably.

Note that, the maximum radial strain does not occur at the vicinity of tunnel walls in the simulation, which is different from the observation of experimental tests (shown in Fig. 8(b)). This is mainly owing to the fact that, the ball elements in the first fractured zone (adjacent to the tunnel wall) have been squeezed after tension, thus they still link together through contact bonds (without strength) instead of spalling. By contrast, due to the brittleness of rock mass, some fragments broke off from the tunnel walls (spalling) in the experimental tests, thereby producing larger radial displacements. Despite this discrepancy, the resulting disintegration patterns produced by DLSSM are acceptable.

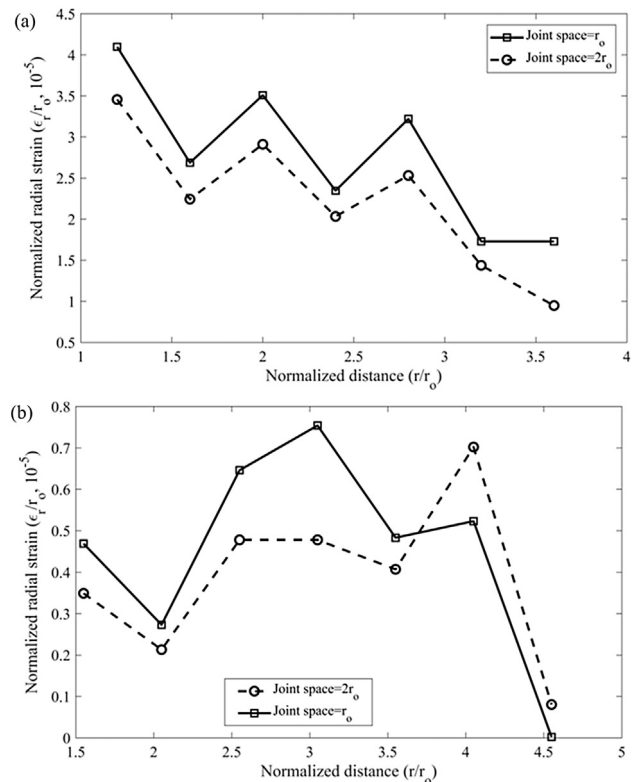


Fig. 8. Comparison of normalized radial strains (left side) with different joint spaces: (a) laboratory model testing results (Zhang et al., 2014), and (b) numerical results.

3. Zonal disintegration processes of tunnels with different shapes and heterogeneities

3D numerical models with different tunnel shapes, sizes, and

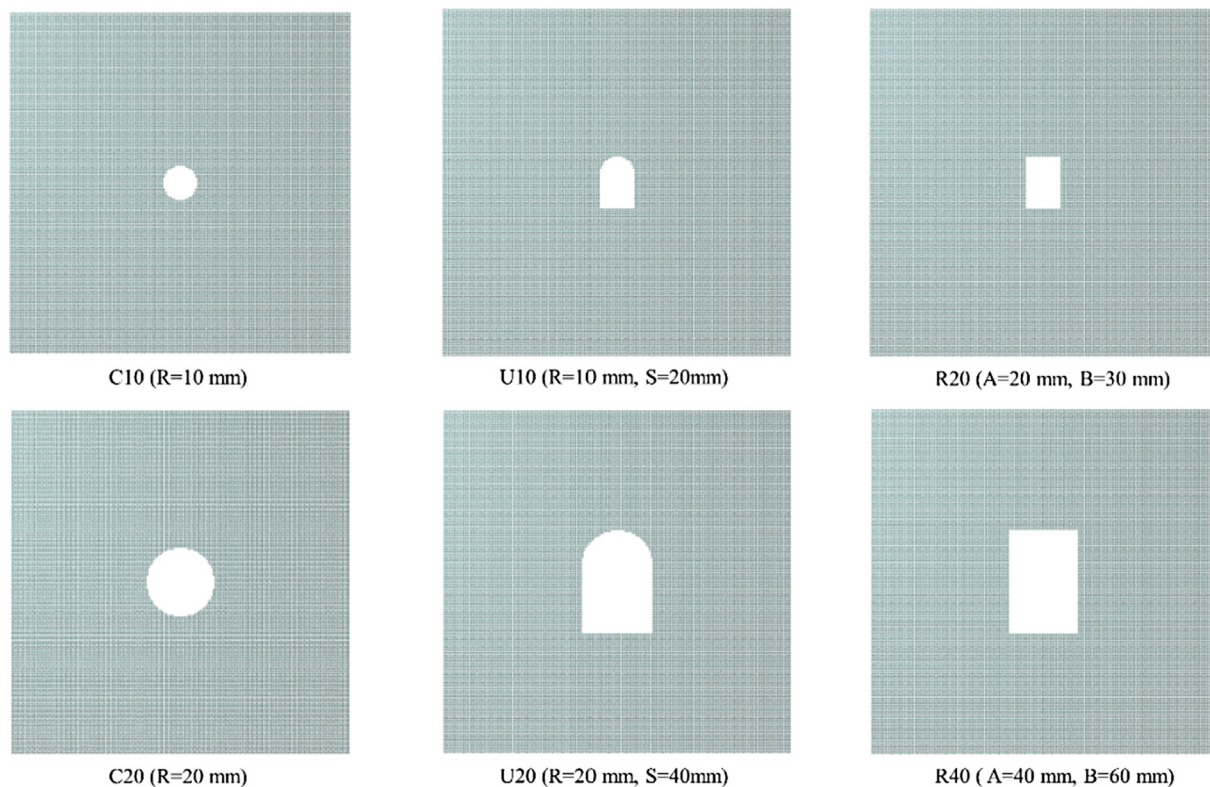


Fig. 9. Numerical models with different tunnel shapes and sizes.

heterogeneity levels are investigated in this study. Three shapes have been considered, namely circular, U-shaped and rectangular tunnels, with two sizes and three heterogeneities being set (shown in Fig. 9). Circular tunnels with radius of 20 mm and 10 mm are named as C20 and C10, respectively. Similarly, U20 and U10 are applied to name U-shaped tunnels with semiarch's radius $R = 20$ mm (square side length $S = 40$ mm) and semiarch's radius $R = 10$ mm ($S = 20$ mm), respectively; and the rectangular tunnels named after their width A : R40 (width $A = 40$ mm, height $B = 60$ mm) and R20 ($A = 20$ mm, $B = 30$ mm) (Fig. 9). Three values of m have been taken to account for the heterogeneity of rock masses: $m = 2$, $m = 5$ and $m = \text{infinity}$ (homogeneous materials, marked as 'H'). The dimension and boundary conditions of all numerical models are the same as that shown in model validation (Section 2, Fig. 2).

In order to describe the progressive failure process of tunnels excavated in deep zones, fracture patterns at different loading steps have been presented. A few important steps have been chosen, e.g., the initiation of the first fracture ring, extension of this ring, then the appearance of the second fracture ring, extension of the second fracture zone, etc. Note that, owing to the different mechanical properties, distribution of weak joints and other influence factors, the fracturing process and its corresponding fracture pattern may vary from case to case (under the same loading speed).

3.1. Numerical simulation for zonal disintegration of circular tunnels with different heterogeneities

The processes of zonal disintegration for circular shaped tunnels with radius of $R = 10$ mm are depicted in Fig. 10, in which the fracture zones are demonstrated both explicitly with broken fields (Fig. 10(a)) and implicitly with maximum principle strain (Fig. 10(b)). For homogeneous material model C10 (H), the first circular fracture zone appears around the tunnel border at Step 130, this fracture zone (tension cracking) expands parallel to the tunnel profile with further loading (Step 150), where compressed streak lines appears at four corners of the

main fracture zone. These compressed lines expand and propagate to form a compression circle (Step 165), enclosing the first main fracture zone. Meanwhile, a small inner compressed zone parallel to the tunnel profile is formed, dividing the first main fracture zone into two sub-fracture zones, with the smaller one adhering to the tunnel wall and the larger one lying between two compression zones. Thus, the process of zonal disintegration has been illustrated explicitly with the broken zones. With further loading steps (Step 210), the main tension broken zone (red area) expands to a larger intact region where intact rock masses around the tunnel tend to crack, at the mean time the inner compression zone (green area) extends to domain some regions of the main fracture zone (red area). This is attributed to the broken of connection bonds between ball elements in the intact region and the establishment of contact bonds between ball elements in the tension cracking zones. The process of zonal disintegration also has been illustrated by the alternate appearance of tension zones and compression regions in Fig. 10(b) for C10 (H) model. These tension and compression zones are corresponding to tension fracturing rings and compression circles shown in Fig. 10(a), the borders of which are also highlighted by different colours in Fig. 10(b).

For heterogeneous rocks ($m = 5$ and $m = 2$), the main characteristics of the alternately appeared fracture patterns and compression fields are similar to that of homogeneous rock mass (Fig. 10(a)). Note that, due to the inherent heterogeneity, tortuous fracture zones have been observed. Also, the number of loading steps for the occurrence of the first fracture zone is smaller for heterogeneous rocks, 130 for C10 (H), 120 for C10 ($m = 5$) and 100 for C10 ($m = 2$). This means that, with the same horizontal displacement along the tunnel axis being applied, tunnels in heterogeneous rock masses have a higher probability of zonal disintegration. However, the final fracture patterns and the propagation of both tension cracking zones and compression fields vary upon the variation of heterogeneities. This means that the higher the homogeneous index, the more regular the fracture (compression) rings, and vice versa. This process also has been presented by the maximum principal strain as shown in Fig. 10 (b). It is noted that, for

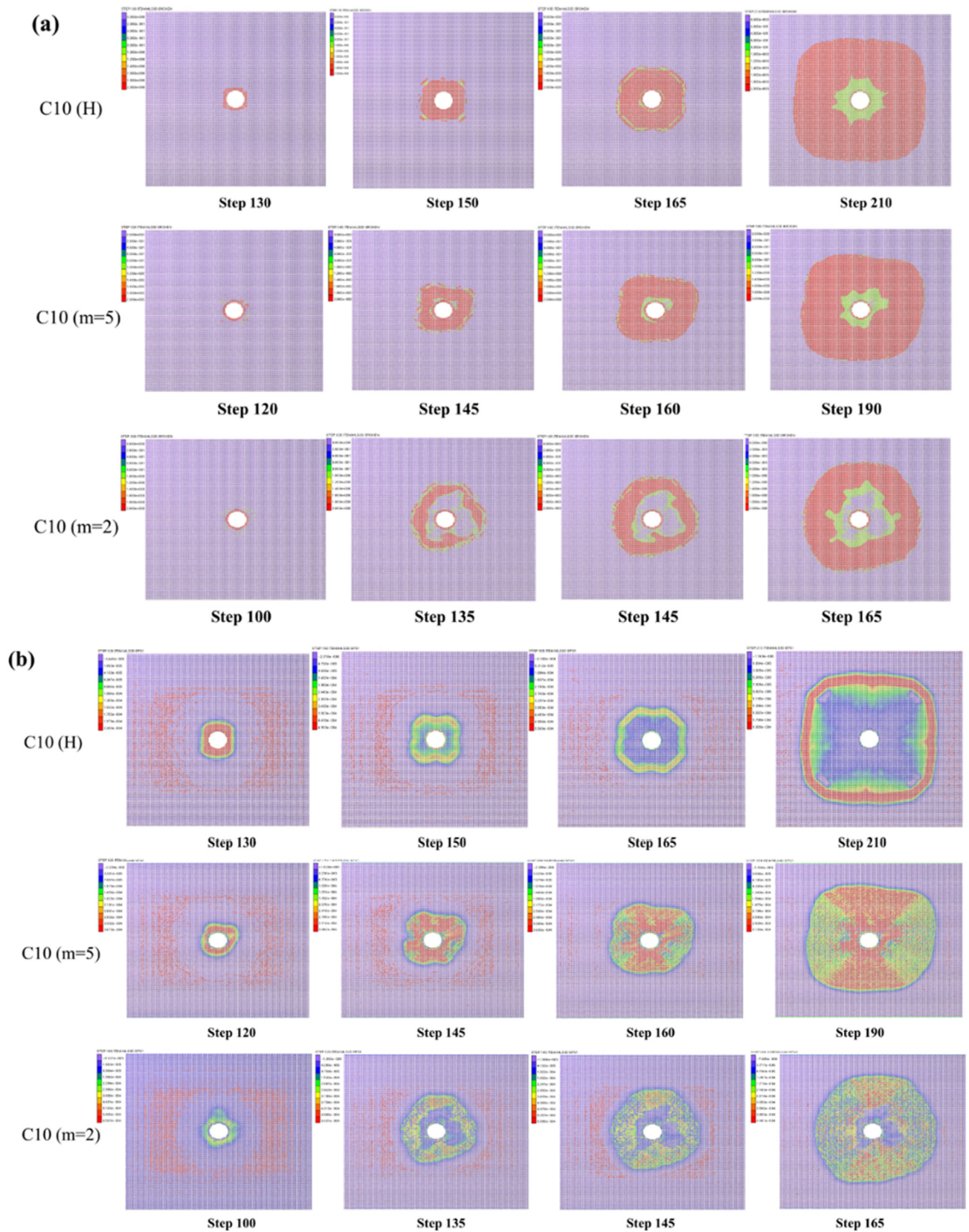


Fig. 10. The process of zonal disintegration for circular shaped tunnels ($R = 10$ mm) with different heterogeneities (H , $m = 5$ and $m = 2$): (a) broken fields, and (b) maximum principle strain. For the contour map of maximum strain, colours range from purple to red colour, corresponding to compression zones to tension zones. (For interpretation of the references to colour in this figure legend, the reader is referred to the web version of this article.)

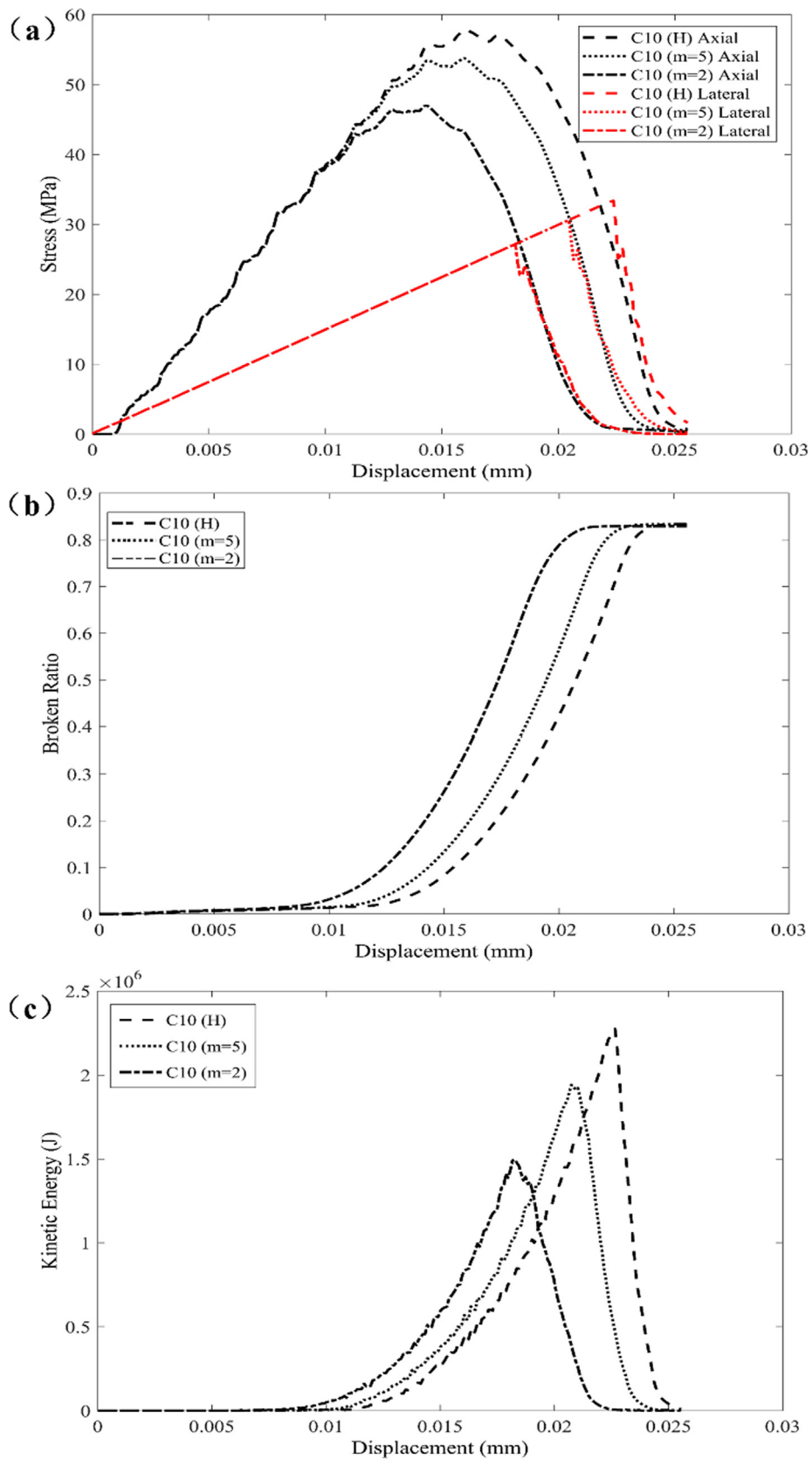


Fig. 11. Responses of stresses, broken ratio and kinetic energy during zonal disintegration for C10 tunnels with different heterogeneities: (a) axial stress and lateral stress-displacement curves; (b) broken ratio-displacement curves; and (c) kinetic energy-displacement curves.

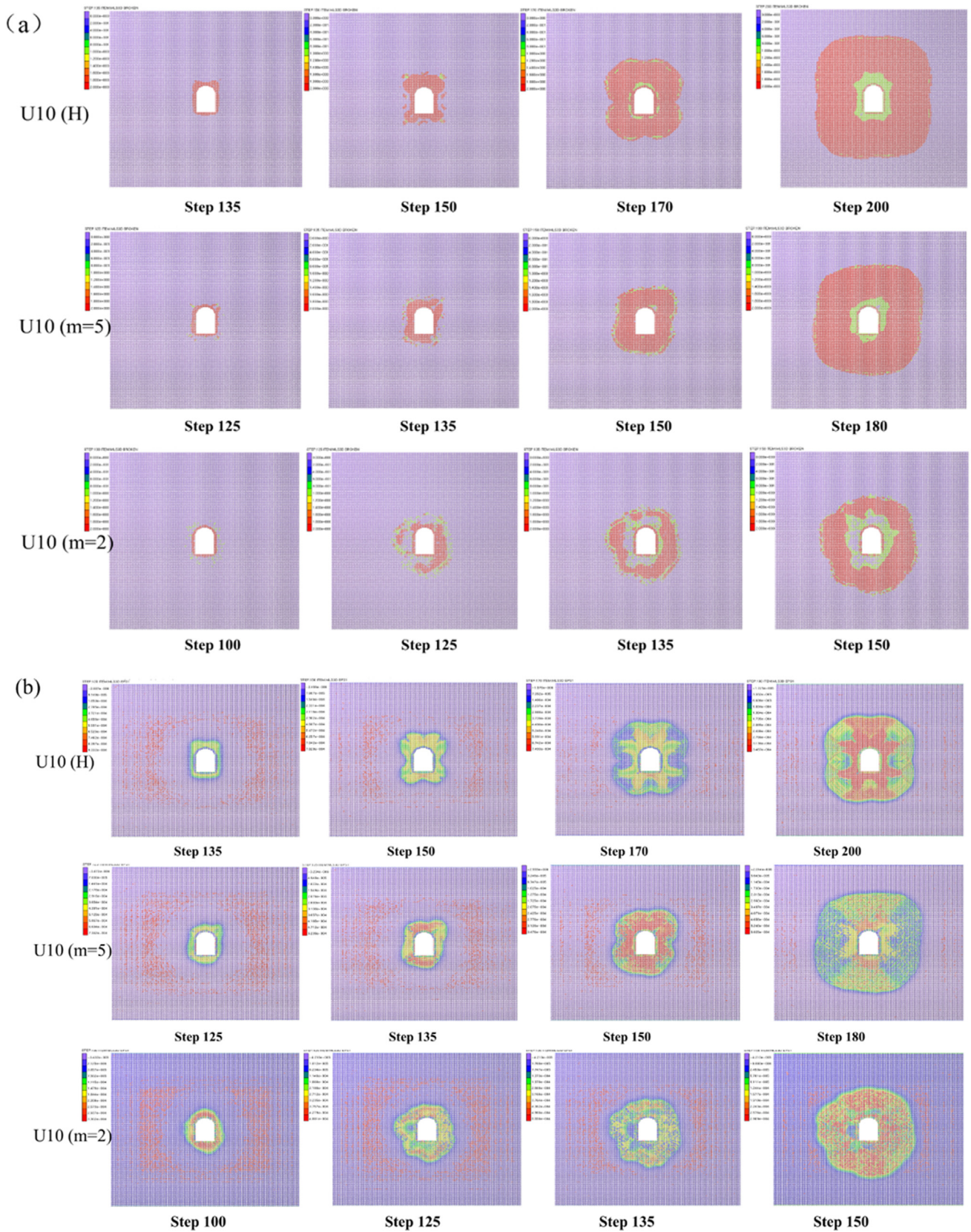


Fig. 12. The process of zonal disintegration for U shaped tunnels ($R = 10$ mm) with different heterogeneities (H , $m = 5$ and $m = 2$): (a) broken fields, and (b) maximum principle strain.

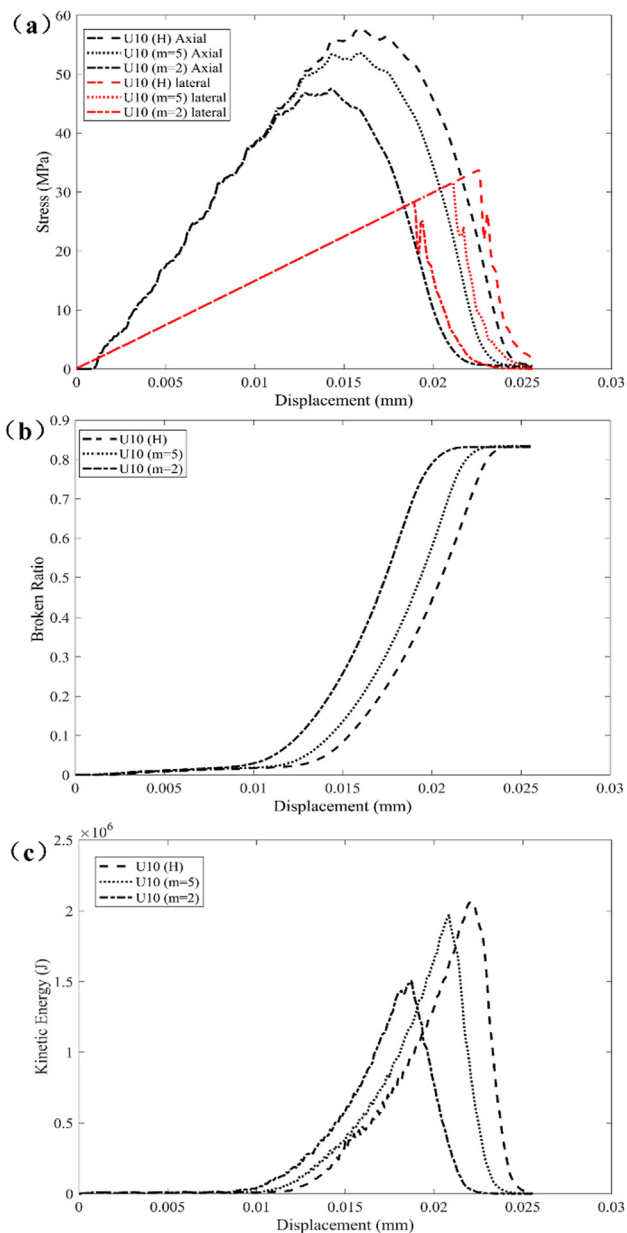


Fig. 13. Responses of stresses, broken ratio and kinetic energy during zonal disintegration for U10 tunnels with different heterogeneities: (a) axial stress and lateral stress-displacement curves; (b) broken ratio-displacement curves; and (c) kinetic energy-displacement curves.

rock mass with $m = 2$, an irregular intact zone has been observed between the first compression zone and the first appeared fracture zone beside the tunnel wall. Thus, five irregular zones appear alternately from the tunnel wall to its far field, namely, the first slim fracture zone, intact zone, compression zone, the main fracture zone and the slim compression zone on the border of the outer intact zone. This demonstrates that zonal disintegration has been influenced by the heterogeneity of rock masses.

For a better analysis of the numerical results, the axial and lateral stresses, broken ratio, and kinetic energy versus axial displacement curves are plotted in Fig. 11. Overall, the mechanical response of all models are relatively elastic brittle. The residual states for all models are characterised by an ultimate value in broken ratio (0.823), approaching which both the kinetic energies and the lateral compression stresses reach to their peaks. Interestingly, the first fracture zones form when the axial compression stresses reach to around 85% of their

strengths; broken ratios increase slowly before the occurrence of the first fracture zones, beyond such points (Step 100 for $m = 2$, Step 120 for $m = 5$ and Step 130 for H) broken ratios (around 0.04) grow dramatically. Note that, when the broken ratios approximately approach 0.2 (Step 145 for $m = 2$, Step 160 for $m = 5$ and Step 165 for H), the stress-displacement curves reach to their peak strength points, corresponding to the final completed patterns of zonal disintegration for all models. Thus, essential support should be activated before the peak stress points for the consideration of tunnel's safety. It is worth noting that the peak points of lateral compression stresses appear simultaneously with the occurrence of maximum kinetic energy releases due to the tendency of model collapse. While, the lateral peak compression stresses appear later than their corresponding axial peak compression stresses, which shows some time lag effects on two principle stresses. Therefore, the collapse of tunnel structure may happen if the lateral stress goes beyond its peak stress, which also can serve as the indicator of failure in deep tunnels.

Inspection of the compressive stress-displacement (Fig. 11(a)) and kinetic energy-displacement curves (Fig. 11(c)) demonstrates that, C10 (H)-the homogeneous model has the highest peak values on both compressive strength and kinetic energy, and C10 ($m = 2$) model is featured with the lowest values in both figures. For C10 ($m = 2$), the broken ratio (Fig. 11(b)) and kinetic energy (Fig. 11(c)) increase faster than those recorded in C10 (H and $m = 5$). Therefore, during the process of zonal disintegration a relative homogeneous material has a relatively higher values in compressive strength (as well as kinetic energy) and a lower increasing rate in broken ratio before model collapse, and vice versa.

3.2. Numerical simulation for zonal disintegration of U-shaped tunnels with different heterogeneities

Fig. 12(a) depicts the zonal disintegration processes explicitly through broken zones for U-shaped tunnels U10s (semiarch radius = 10 mm) with different heterogeneities (H , $m = 5$ and $m = 2$). Similar to the circular tunnels, the first main fracture fields form along the tunnel profile (Step 135 for H , Step 125 for $m = 5$ and Step 100 for $m = 2$). Then the first fracture zones of U10 (H and $m = 5$) expand outwards to further intact areas with larger tension cracking zone being observed around the semiarch and two corners of tunnels (Step 150 for H and Step 135 for $m = 5$). While, for heterogeneous model (Step 125 for $m = 2$), the first fracture zone propagates to the intact rock masses of the right side wall and tunnel bottom, leaving 3 intact areas (around the semiarch, the left wall and the left corner) enclosed by an irregular compression ring. With further loading (Step 170 for H , Step 150 for $m = 5$ and Step 135 for $m = 2$), the compression stresses in the axial direction reach to their peaks (Fig. 13 (a)) and all tunnel models are featured with different patterns of zonal disintegration. This is understandable, due to local heterogeneity the broken fields and compression zones propagate more tortuously, thus leading to different fracture patterns (compression zones and intact zones between them) in Fig. 12(a) and different principal train contour maps in Fig. 12(b) as well.

Similar to circular tunnels, the loading step number for the occurrence of first fracture zone varies on the homogeneous level, with larger numbers being observed for relative homogeneous material. This complies with the stress-displacement curves shown in Fig. 13(a). Relatively homogeneous material is characterised by higher compression strength and kinetic energy release (Fig. 13(c)), and with the same loading step it has the lower value in broken ratio before the residual state, and vice versa. In addition, the final complete patterns of the zonal disintegration have been observed when the axial compression stresses reach to around 85% of their strengths. It is noted that the lateral stress and kinetic energy rise up to their peak points at the same loading step for the U-shaped tunnels, which show some similarities to these observations in Fig. 11 for circular tunnels.

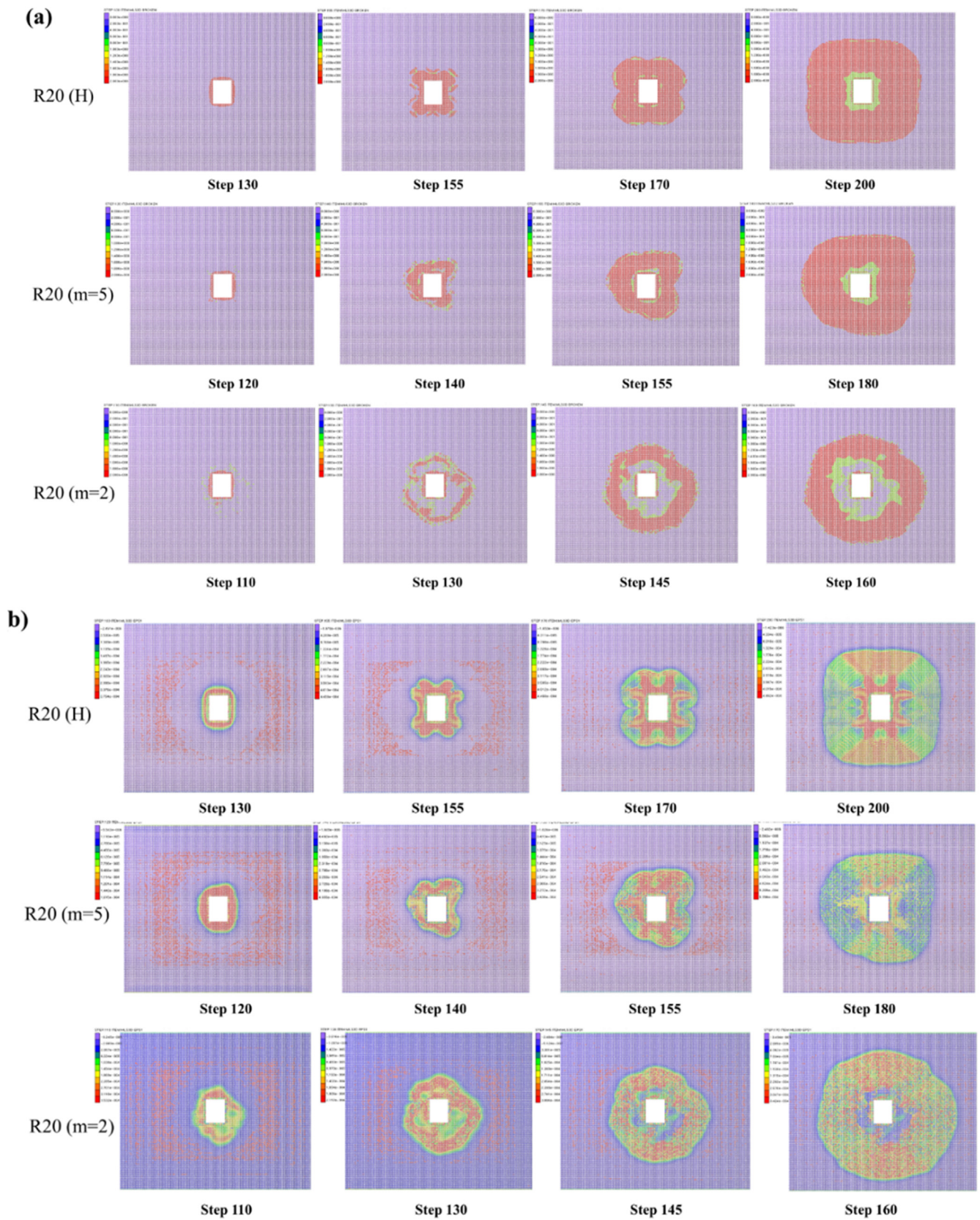


Fig. 14. The process of zonal disintegration for rectangular tunnels ($A = 20 \text{ mm}$, $B = 30 \text{ mm}$) with different heterogeneities (H , $m = 5$ and $m = 2$): (a) broken fields, and (b) maximum principle strain.

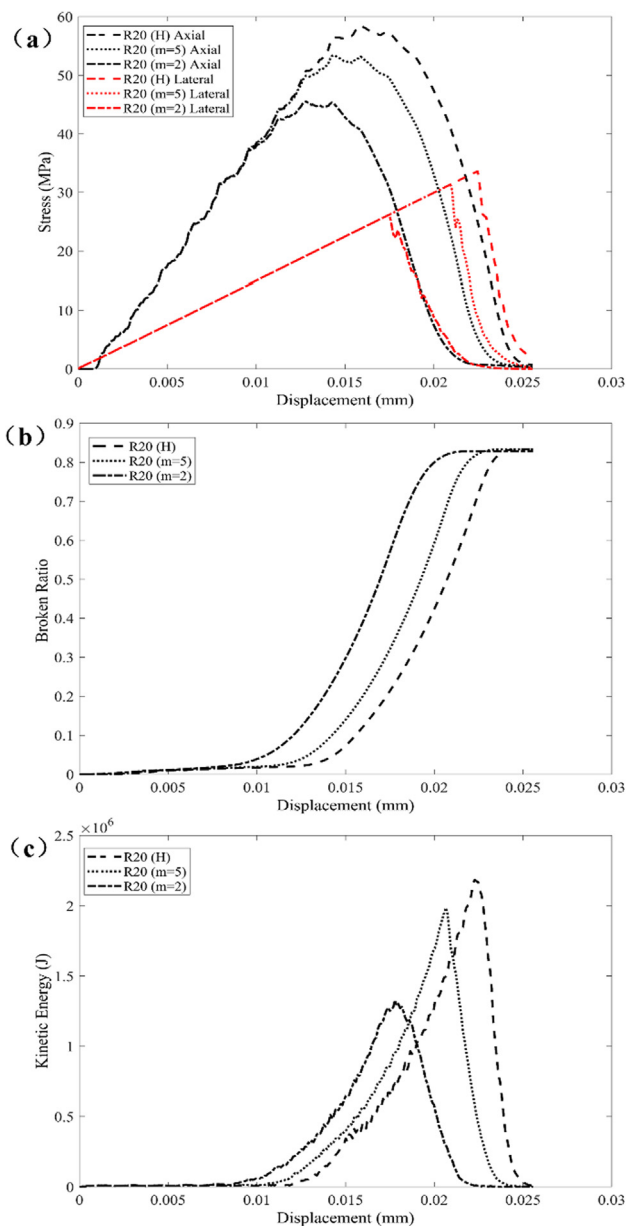


Fig. 15. Responses of stresses, broken ratio and kinetic energy during zonal disintegration for R20 tunnels with different heterogeneities: (a) axial stress and lateral stress-displacement curves; (b) broken ratio-displacement curves; and (c) kinetic energy-displacement curves.

3.3. Numerical simulation for zonal disintegration of rectangular tunnels with different heterogeneities

Zonal disintegration processes of rectangular tunnels ($A = 20$ mm and $B = 30$ mm) with different heterogeneities are illustrated in Fig. 14. The main characteristics of zonal disintegration are almost the same as those observed in circular and U-shaped tunnels. Fig. 14 (a) shows that the first fracture zones in 3 models are almost the same: in the first stage (Steps 130 for H , 120 for $m = 5$ and 110 for $m = 2$) the main fracture zones appear at the four sides of the rectangular excavations, with many small compression zones forming around the fracture regions of heterogeneous materials ($m = 5$ and 2). As loading increases (Steps 155 for H , 140 for $m = 5$ and 130 for $m = 2$), these broken zones propagate outwards. Specifically, homogeneous model is characterised by larger tension zones around four corners due to the coalescence of the two pairs of sub-fracture zones, which is similar to the fracture

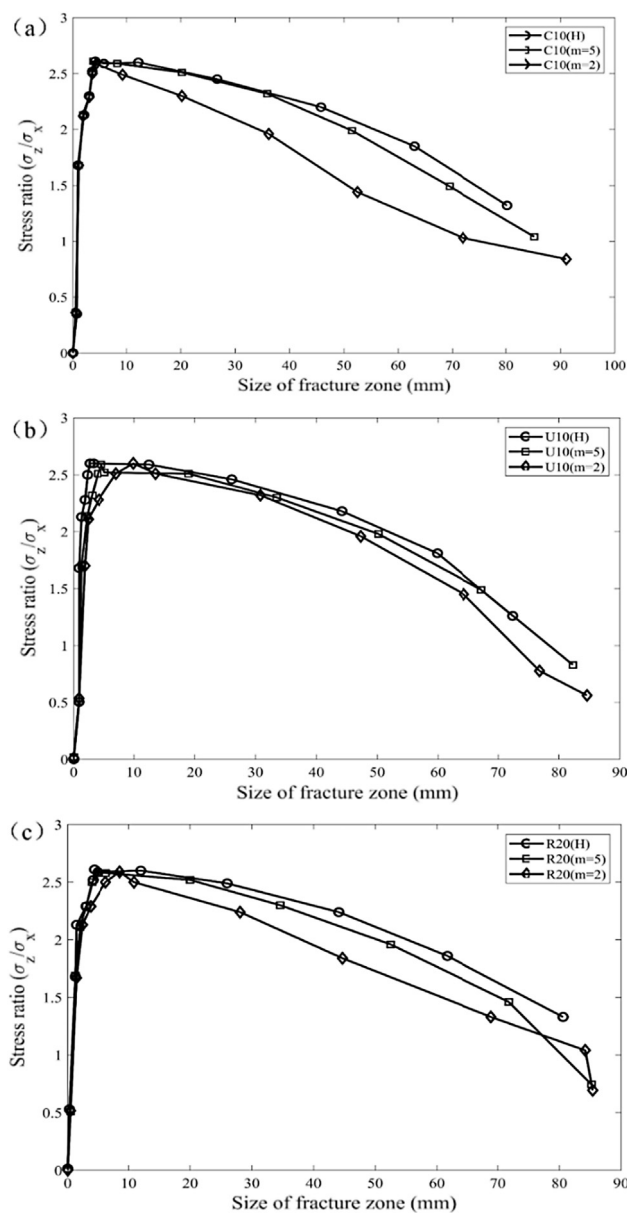


Fig. 16. Stress ratio versus fracture zone propagation for three shaped tunnels with different heterogeneities: (a) circular tunnel C10, (b) U-shaped tunnel U10, and (c) rectangular tunnel R20.

patterns of U-shaped tunnels (U10 (H) in Fig. 12(a)). For heterogeneous models, the expansion of the first fracture zone and the alternative appearance of tension cracking-compression zones (and intact zones) depends on both the level of heterogeneities and the local heterogeneities. These irregular shaped fracture zones and thin compression/intact zones in R20 ($m = 5$ and 2) comply with the fracture patterns discussed for U10 and C10 ($m = 5$ and $m = 2$), where the lower the homogeneous index, the more tortuous their fracture and compression zones. Note that the intact zone only can be observed with the homogeneous index of $m = 2$. Similarly, the final zonal disintegration patterns have been identified when the stresses in axial direction approach their peaks (Fig. 15(a)), and the material models go into their residual states when their broken ratios reach to the ultimate value. Similar to Fig. 11(C10) and 11 (U10), Fig. 15 also demonstrates that homogeneous material is characterised by the higher compression strength and kinetic energy release, and with the same loading step it has a lower value in broken ratio before the residual state, and vice versa.

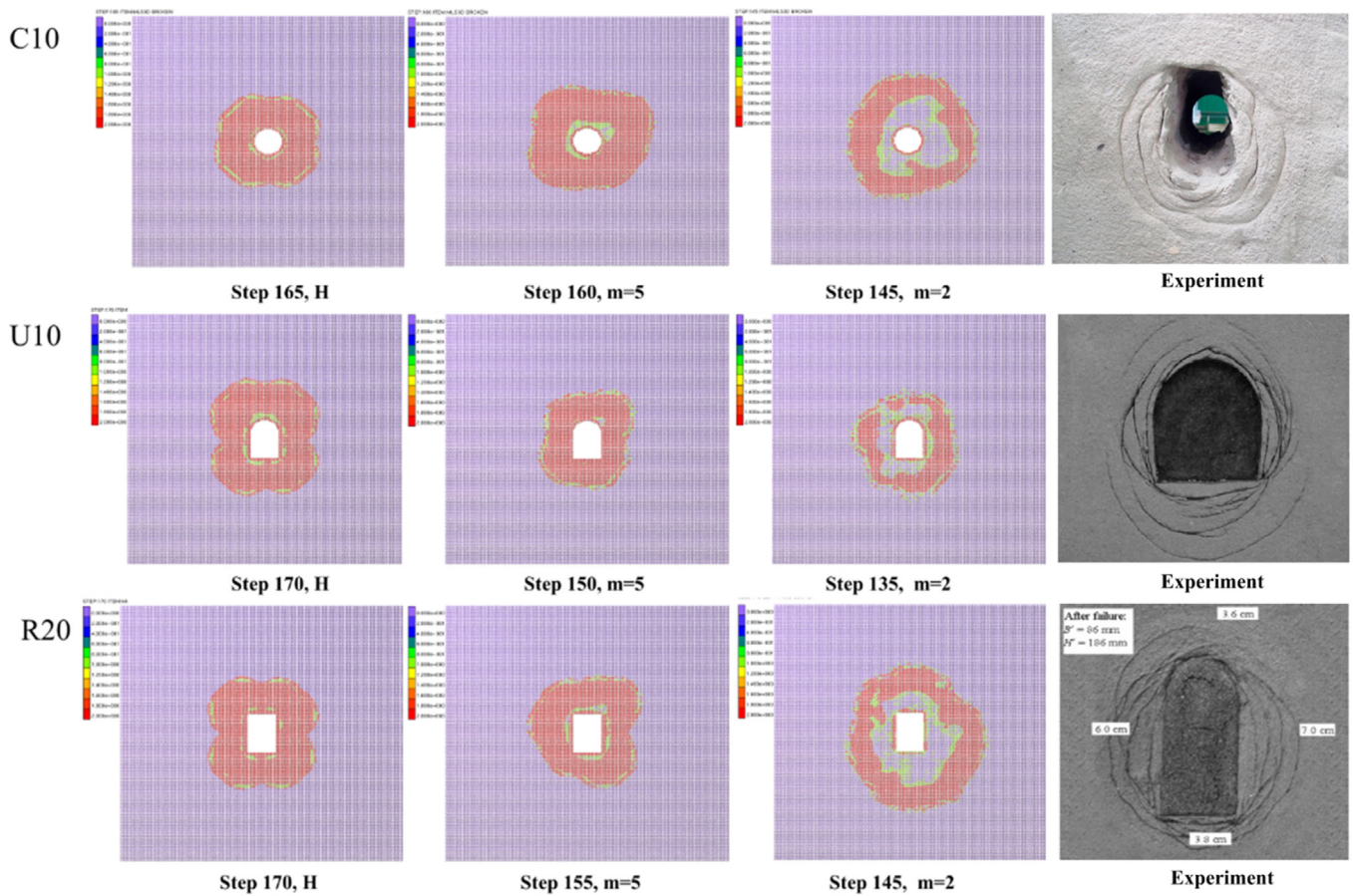


Fig. 17. Final patterns of zonal disintegration for different shaped tunnels (C10, U10 and R20) with different heterogeneities (H , $m = 5$ and $m = 2$), and experimental model tests (circular tunnel from (Zhang et al., 2017), U-shaped tunnel from (Yuan et al., 2014), and rectangular tunnel from (Gu et al., 2008)).

3.4. The process and mechanisms of zonal disintegration

As demonstrated in Sections 3.1–3.3, the process of zonal disintegration starts from the first tension cracking zone around the border of openings in all cases with different shapes and heterogeneities. And the first fracture zones occur when the axial compressive stresses approximately get close to 85% of their compression strengths (stress ratio approaching 2.6, as shown in Fig. 16), which can be seen as the special in-situ stress condition for zonal disintegration in deep rock masses. With loading increasing, the first fracture ring expands and propagates outwards due to the tension failure of surrounding ball elements. This can be explained by the constitutive law adopted in DLSM, ultimate tension strain has been achieved in these fracture zones as the displacements between adjacent ball elements reach to the ultimate value which is calculated based on the material strength. Then, two more fracture zones appear, enclosing two compression (on intact zone for $m = 2$) zones. These compression zones are formed due to ultimate compressive strain achieved locally, and the ball elements in these compressed broken fields are connected by contact bonds with zero strengths as explained in the constitutive law for compression failure. The final zonal disintegration pattern is achieved when the axial compression stress approaches the peak point, beyond which the tension cracking zone continues to expand, then the compression stress drops suddenly and the material model goes into residual state with maximum broken ratio being reached (off-peak stage in the stress ratio (σ_z/σ_x)-fracture zone size plot in Fig. 16). This is the process of zonal disintegration, which has been explicitly reproduced by DLSM. For homogeneous materials, these fracture zones are formed due to local stress concentration. The tension cracking zone is normally found to have large tension strains, while the compression zone is associated

with large compression strain. These two types of strains alternately appear (wavy distribution profiles of radial displacement in Fig. 4), corresponding to the alternate occurrence of tension and compression zones. For heterogeneous material model, irregular shaped fracture zones are observed enclosing the excavation owing to the fact that broken fields propagate with the preference to some areas with low strength or weakness (Ma and Zhao, 2015; Tang et al., 2000). This may be applied to explain the final patterns of zonal disintegration which is characterised by irregular shaped tension, compression and intact zones. Also, the smaller the homogeneous index (more heterogeneous), the more tortuous the fracture/compression zones, the lower the compression strength, and the faster the broken ratio increment during the process of zonal disintegration. This may be explained by the adoption of strength/failure criteria.

To figure out the threshold value of homogeneous index m for the occurrence of zonal disintegration, $m = 1.5$ and $m = 1.75$ have been applied to the rock masses, in which three typical shaped tunnels are excavated. However, no zonal disintegration has not been found, which demonstrates that zonal disintegration would not occur in tunnels built in highly heterogeneous or weak rock masses.

For the purpose of further demonstrating the effects of heterogeneities on the process of zonal disintegration, stress ratio (σ_z/σ_x) versus fracture zone propagation (averagely) for all cases are plotted in Fig. 16. It is apparently that, fracture zones forms soon after the stress ratio approaching 2.6 (around the peak point), it drops gradually with fracture zone propagation. In all cases, the pre-peak response of stress ratio-fracture zone propagation are all most the same, and they diverge after peak points. That is, the stress ratio descents faster in the case of more heterogeneous rock mass than its counterparts, which also comply with the stress-displacement responses of all cases in previous sections

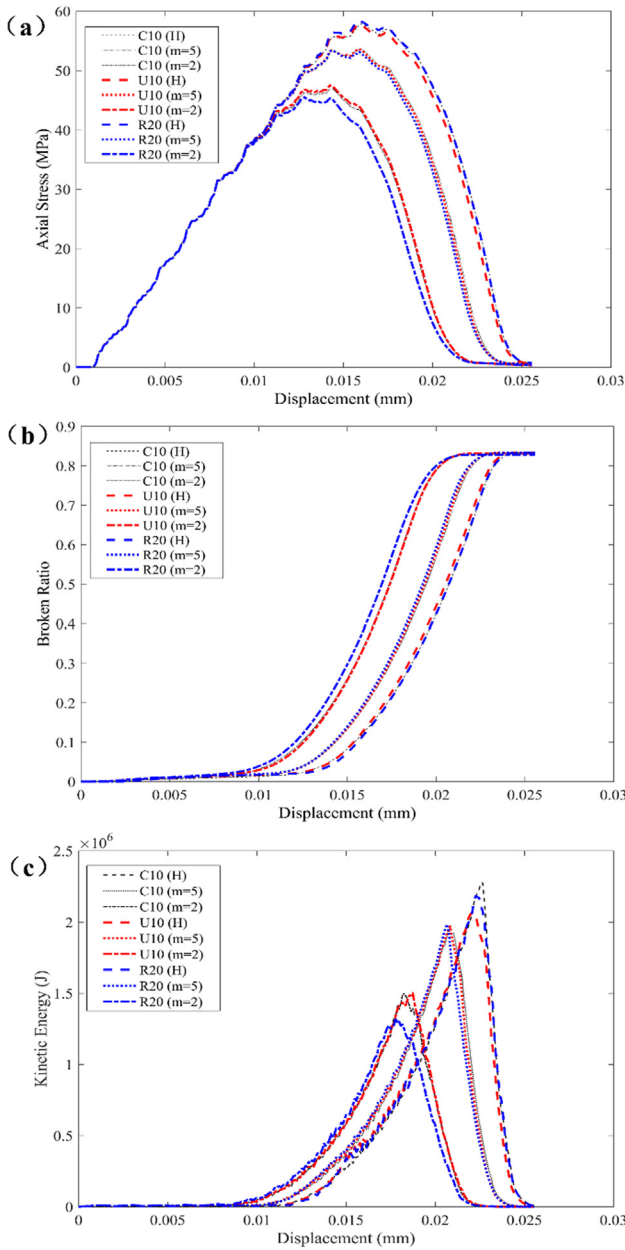


Fig. 18. Responses of stresses, broken ratio and kinetic energy during zonal disintegration for three typical shaped tunnels with different heterogeneities: (a) axial stress-displacement curves; (b) broken ratio-displacement curves; and (c) kinetic energy-displacement curves.

(Figs. 11, 13 and 15). The plot of stress ratio-size of fracture zone also explicitly suggests that, essential measures should be taken to prevent further propagation of fracture zone when stress ratio approaching its peak. Also, the off-peak stage of stress ratio-size of fracture zone is not stable, as fracture zone keeps expanding outwards even though the stress ratio descends dramatically.

4. Discussions

4.1. Shape effects on zonal disintegration

The final patterns of zonal disintegration for 3 typical shaped tunnels with different heterogeneities are compared with experimental model results in Fig. 17. Overall, the final patterns of heterogeneous materials with $m = 2$ match with experimental model tests better and

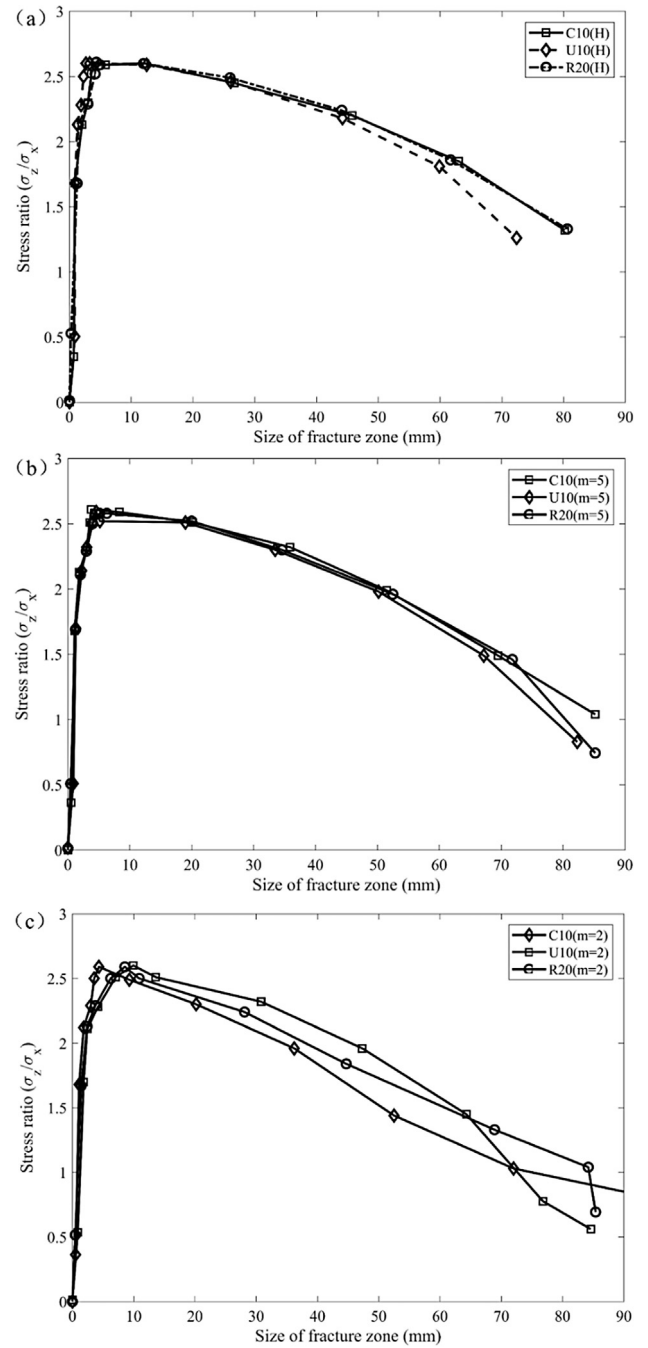


Fig. 19. Stress ratio versus fracture zone propagation for three shaped tunnels with different heterogeneities: (a) homogeneous materials (H), (b) $m = 5$, and (c) $m = 2$.

reasonably. For homogeneous material models, the circular shaped tunnel (C10 (H)) is characterised by alternate occurrence of fracture-compression rings; while in U-shaped and rectangular tunnels (U10 (H) and R10 (H)), the main fracture and compression zones are found to be with flower patterns due to the coalescences of sub-fracture zones and sub-compression regions at four corners. For heterogeneous materials ($m = 5$ and 2), irregular shaped fracture-compression-intact rings have been observed owing to the distribution of local weakness. With the decreasing in homogeneous index, these broken-intact zones become more tortuous. This implies that different tunnel shapes would lead to different patterns of zonal disintegration for homogeneous rocks, while the final disintegration patterns of heterogeneous materials would depend on both the tunnel shape and its heterogeneous level, including

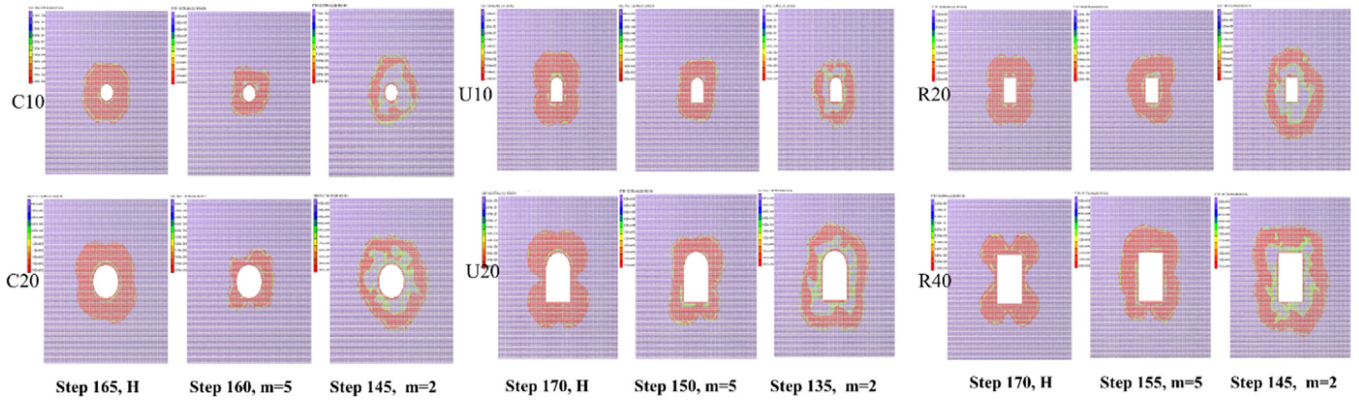


Fig. 20. Final patterns of zonal disintegration for different shaped tunnels (C10-C20, U10-U20 and R20-R40) with different heterogeneities and sizes (H , $m = 5$ and $m = 2$).

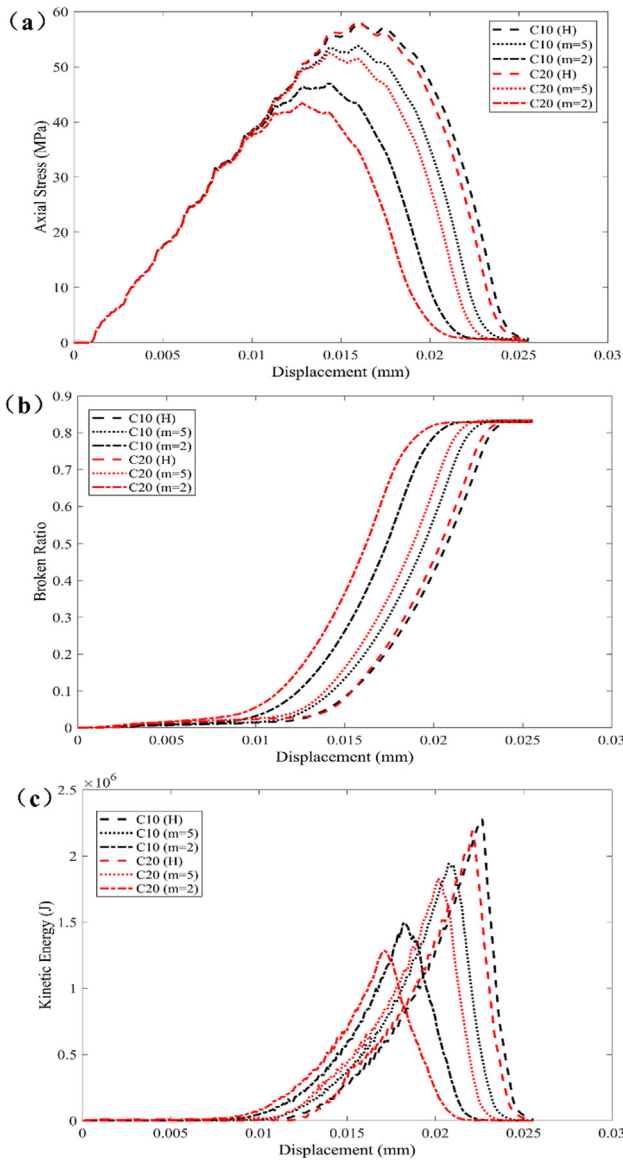


Fig. 21. Responses of stresses, broken ratio and kinetic energy during zonal disintegration for circular tunnels with different heterogeneities and sizes: (a) axial stress-displacement curves; (b) broken ratio-displacement curves; and (c) kinetic energy-displacement curves.

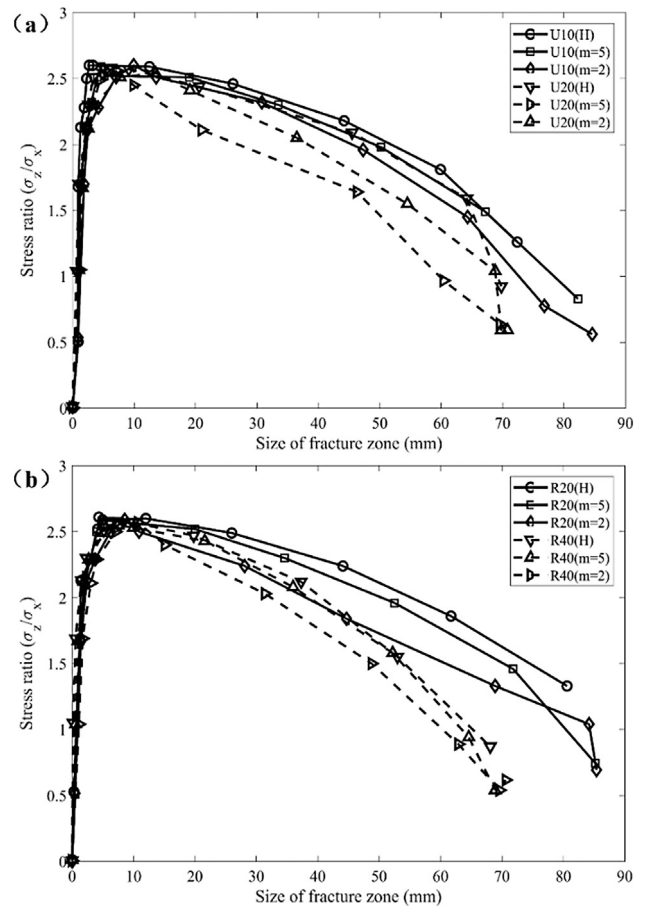


Fig. 22. Stress ratio versus fracture zone propagation for tunnels with different heterogeneities, (a) U-shaped tunnels, and (b) Rectangular tunnels.

the homogenous index and the distribution of local weakness. The compressive stress, broken ratio and kinetic energy release versus displacement curves are depicted in Fig. 18 for further analysis. As can be seen, the responses of compression stress, broken ratio and kinetic energy release in three shaped tunnels are very close with only tiny differences being observed for rectangular shaped tunnels. This indicates that tunnel shape would have very limited influences on the responses of kinetic energy release, broken ratio and compressive stress-displacement. Similar phenomenon also can be found in the responses of stress ratio-fracture zone propagation (Fig. 19). This reveals that the tunnel shape may not affect the response of stress ratio-fracture zone propagation significantly. In addition, tunnel shape has very little

influence on the size of final fracture zone in all cases considered.

4.2. Size effects on zonal disintegration

The final patterns of zonal disintegration for 3 typical shaped tunnels with different sizes and heterogeneities are compared in Fig. 20. The responses of stresses, broken ratio and kinetic energy during zonal disintegration for circular tunnels with different heterogeneities and sizes are plotted in Fig. 21. Overall inspection of these zonal disintegration patterns reveals that, larger sized tunnels are featured with larger fracture rings and compression/intact zones. Accordingly, the compressive strength and kinetic energy release for a larger opening in the same rock masses are lower than the smaller ones; and the broken ratios of larger sized tunnels increase faster than their counter parts with the same loading steps before the model collapse (Fig. 21). For homogeneous material models, the U-shaped and rectangular tunnels with a larger size (U20 (*H*) and R20 (*H*)) are characterized by larger and more outstanding coalescence fracture zones compared with their counter parts, due to the coalescences of larger sub-fracture zones and sub-compression regions at four corners of these tunnels. Coalesces of sub-fracture zones formed at four corners are mainly due to shear cracking in the vicinities of corner areas for tunnels with non-curved profiles. For heterogeneous materials ($m = 5$ and 2), owing to the random distribution of local weakness, larger irregular shaped fracture-compression-intact rings around the openings with larger sizes have been observed. The size effects of circular tunnels vary with their homogeneous indexes- m . As shown in Fig. 21, in terms of compression strength, energy release and broken ratio, the gaps between small (C10) and large sized tunnels (C20) decrease with an increasing in homogeneous index m .

For the purpose of further demonstrating the size effects on the process of zonal disintegration, stress ratio (σ_z/σ_x) versus fracture zone propagation (averagely) for rectangular and U-shaped tunnels are plotted in Fig. 22. Obviously, the pre-peak response of stress ratio versus fracture zone propagation are almost the same for all cases. In the post peak stage (the stage of unstable fracture zone extension), stress ratio drops faster in rock mass with larger size of excavation, complying with the stress-displacement responses of all cases in Fig. 22. This indicates that, deep excavated tunnels with a larger size may be characterised by ongoing zonal disintegration with a relevant lower in-situ stress ratio, implying that a larger size opening excavation may be less stable compared with the excavation of a smaller size opening.

5. Conclusions

The main characteristics of zonal disintegration for tunnels with different shapes, sizes and heterogeneities have been investigated through DLSM. Reasonable agreement between numerical results and laboratory model tests illustrates that, applying the displacement loading along the longitudinal axis of a tunnel would reproduce the phenomenon of zonal disintegration. The occurrence of zonal disintegration mainly depends on the material heterogeneities and the in-situ stress level. The fracture patterns formed during zonal disintegration rely on the tunnels' shape, size, the heterogeneity level and the distribution of local weakness in the surrounding rock mass. Thus, DLSM is a powerful numerical tool to explicitly reproduce zonal disintegration within deep rock mass with different joint spaces.

Numerical investigation on the influencing factors of zonal disintegration demonstrates that, a relatively homogeneous material has a higher compression strength and a larger kinetic energy release at the model failure. Accordingly, it has a lower broken ratio under the same loading step before material collapse. In addition, tunnels with larger sizes are featured with larger fracture rings and compression/intact zones, corresponding to lower values in compressive strength (as well as kinetic energy release) and larger broken ratios under the same loading steps before the model collapse. The main fracture zones in

circular tunnels are regular fracture rings; while in U-shaped and rectangular tunnels flower patterns are found due to the coalescence of sub-fracture zones at four corners of tunnels. However, tunnel shape has very little influence on both the size of final fracture zone and the mechanical responses of rock mass in all cases.

Acknowledgements

This work is supported by National Natural Science Foundation of China (NSFC, NO. 51708564, 51678578, and 51508416), Guangdong Natural Science Foundation (GNSF, NO. 2016A030313233), and Guangzhou Science & Technology Program (GSTP, NO. 201704020139). The financial support is gratefully acknowledged. Constructive comments from anonymous reviewers and Prof. Gao-Feng Zhao (Tianjin University, China) is also acknowledged.

Declarations of interest

None.

Appendix A. Supplementary material

Supplementary data to this article can be found online at <https://doi.org/10.1016/j.tust.2019.04.017>.

References

- Adams, G.R., Jager, A.J., 1980. Petroscopic observations of rock fracturing ahead of stope faces in deep-level gold mines. *J. South African Instit. Min. Metall.* 80, 204–209.
- Borzykh, A.F., 1990. Features of the zonal disintegration of roof rocks and a coal seam around mine workings. *Soviet Min.* 26, 418–427. <https://doi.org/10.1007/BF02499559>.
- Chen, X., Li, T., Xu, J., Li, Y., 2017. Mechanism of zonal disintegration phenomenon (ZDP) and model test validation. *Theor. Appl. Fract. Mech.* 88, 39–50. <https://doi.org/10.1016/j.tafmec.2016.11.007>.
- Gu, J., Gu, L., Chen, A., Xu, J., Chen, W., 2008. Model test study on mechanism of layered fracture within surrounding rock of tunnels in deep stratum. *Chin. J. Rock Mech. Eng.* 27, 433–438 (in Chinese).
- Guzev, M.A., Paroshin, A.A., 2001. Non-euclidean model of the zonal disintegration of rocks around an underground working. *J. Appl. Mech. Techn. Phys.* 42, 131–139. <https://doi.org/10.1023/A:1018877015940>.
- Jia, P., Yang, T.H., Yu, Q.L., 2012. Mechanism of parallel fractures around deep underground excavations. *Theor. Appl. Fract. Mech.* 61, 57–65. <https://doi.org/10.1016/j.tafmec.2012.08.007>.
- Jia, P., Zhu, W., Zhang, S., 2014. Effect of heterogeneity on occurrence of zonal disintegration around deep underground openings. *Int. J. Min. Sci. Technol.* 24, 859–864. <https://doi.org/10.1016/j.ijmst.2014.10.020>.
- Jia, P., Zhu, W.C., 2015. Mechanism of zonal disintegration around deep underground excavations under triaxial stress – Insight from numerical test. *Tunn. Undergr. Space Technol.* 48, 1–10. <https://doi.org/10.1016/j.tust.2015.01.005>.
- Li, S., et al., 2008. In-situ monitoring research on zonal disintegration of surrounding rock mass in deep mine roadways. *Chin. J. Rock Mech. Eng.* 27, 1545–1553.
- Li, S.C., Feng, X.D., Li, S.C., 2013. Numerical model for the zonal disintegration of the rock mass around deep underground workings. *Theor. Appl. Fract. Mech.* 67–68, 65–73. <https://doi.org/10.1016/j.tafmec.2013.11.005>.
- Lin, P., Liu, H., Zhou, W., 2015. Experimental study on failure behaviour of deep tunnels under high in-situ stresses. *Tunn. Undergr. Space Technol.* 46, 28–45. <https://doi.org/10.1016/j.tust.2014.10.009>.
- Lin, P., Zhou, Y., Liu, H., Wang, C., 2013. Reinforcement design and stability analysis for large-span tailrace bifurcated tunnels with irregular geometry. *Tunn. Undergr. Space Technol.* 38, 189–204. <https://doi.org/10.1016/j.tust.2013.07.011>.
- Ma, J., Zhao, G., 2015. Studying the influence of heterogeneity on particle breakage using distinct lattice spring model. *Arab. J. Geosci.* 8, 6595–6621. <https://doi.org/10.1007/s12517-014-1709-z>.
- Qian, Q.H., Zhou, X.P., Yang, H.Q., Zhang, Y.X., Li, X.H., 2009. Zonal disintegration of surrounding rock mass around the diversion tunnels in Jinping II Hydropower Station, Southwestern China. *Theor. Appl. Fract. Mech.* 51, 129–138. <https://doi.org/10.1016/j.tafmec.2009.04.006>.
- Reva, V.N., 2002. Stability criteria of underground workings under zonal disintegration of rocks. *J. Min. Sci.* 38, 31–34. <https://doi.org/10.1023/A:1020236617544>.
- Sellers, E.J., Klerck, P., 2000. Modelling of the effect of discontinuities on the extent of the fracture zone surrounding deep tunnels. *Tunn. Undergr. Space Technol.* 15, 463–469. [https://doi.org/10.1016/S0886-7798\(01\)00015-3](https://doi.org/10.1016/S0886-7798(01)00015-3).
- She, S., Lin, P., 2014. Some developments and challenging issues in rock engineering field in China. *Chinese J. Rock Mech. Eng.* 33, 433–457.
- Shemyakin, E.I., et al., 1987. Zonal disintegration of rocks around underground mines, part III: theoretical concepts. *Soviet Min.* 23, 1–6. <https://doi.org/10.1007/>

- BF02534034.
- Shemyakin, E.I., et al., 1986a. Zonal disintegration of rocks around underground workings. Part II: rock fracture simulated in equivalent materials. *Soviet Min.* 22, 223–232. <https://doi.org/10.1007/BF02500845>.
- Shemyakin, E.I., et al., 1986b. Zonal disintegration of rocks around underground workings, part I: data of in situ observations. *Soviet Min.g* 22, 157–168. <https://doi.org/10.1007/BF02500863>.
- Tang, C.A., 1997. Numerical simulation of progressive rock failure and associated seismicity. *Int. J. Rock Mech. Min. Sci.* 34, 249–261. [https://doi.org/10.1016/S0148-9062\(96\)00039-3](https://doi.org/10.1016/S0148-9062(96)00039-3).
- Tang, C.A., Liu, H., Lee, P.K.K., Tsui, Y., Tham, L.G., 2000. Numerical studies of the influence of microstructure on rock failure in uniaxial compression — Part I: effect of heterogeneity. *Int. J. Rock Mech. Min. Sci.* 37, 555–569. [https://doi.org/10.1016/S1365-1609\(99\)00121-5](https://doi.org/10.1016/S1365-1609(99)00121-5).
- Yuan, L., Gu, J.C., Xue, J.H., Zhang, X.Y., 2014. Model test research on the zonal disintegration in deep rock. *Meitan Xuebao/J. Chin. Coal Soc.* 39, 987–993 (in Chinese).
- Zhang, Q., Jiang, B.S., Wu, X.S., Zhang, H.Q., Han, L.J., 2012. Elasto-plastic coupling analysis of circular openings in elasto-brittle-plastic rock mass. *Theor. Appl. Fract. Mech.* 60, 60–67. <https://doi.org/10.1016/j.tafmec.2012.06.008>.
- Zhang, X.T., Zhang, Q.Y., Xiang, W., Gao, Q., Yuan, S.B., Wang, C., 2014. Model test study of zonal disintegration in deep layered jointed rock mass. *Yantu Lixue/Rock Soil Mech.* 35, 2247–2254 (in Chinese).
- Zhang, Q., Zhang, X., Wang, Z., Xiang, W., Xue, J., 2017. Failure mechanism and numerical simulation of zonal disintegration around a deep tunnel under high stress. *Int. J. Rock Mech. Min. Sci.* 93, 344–355. <https://doi.org/10.1016/j.ijrmms.2017.02.004>.
- Zhao, G.F., 2017. Developing a four-dimensional lattice spring model for mechanical responses of solids. *Comput. Meth. Appl. Mech. Eng.* 315, 881–895. <https://doi.org/10.1016/j.cma.2016.11.034>.
- Zhao, G.F., Fang, J., Sun, L., Zhao, J., 2013. Parallelization of the distinct lattice spring model. *Int. J. Numer. Analyt. Meth. Geomech.* 37, 51–74. <https://doi.org/10.1002/nag.1085>.
- Zhao, G.F., Fang, J., Zhao, J., 2011. A 3D distinct lattice spring model for elasticity and dynamic failure. *Int. J. Numer. Analyt. Meth. Geomech.* 35, 859–885. <https://doi.org/10.1002/nag.930>.
- Zhao, G.F., Zhao, J., 2012. Discontinuum based micromechanics methods. Paper presented at the *Analysis of Discontinuous Deformation Proc. ICADD10*.
- Zhou, X.P., Shou, Y.D., 2013. Excavation-induced zonal disintegration of the surrounding rock around a deep circular tunnel considering unloading effect. *Int. J. Rock Mech. Min. Sci.* 64, 246–257. <https://doi.org/10.1016/j.ijrmms.2013.08.010>.
- Zhou, X.P., Wang, F.H., Qian, Q.H., Zhang, B.H., 2008. Zonal fracturing mechanism in deep crack-weakened rock masses. *Theor. Appl. Fract. Mech.* 50, 57–65. <https://doi.org/10.1016/j.tafmec.2008.04.001>.
- Zhu, Z., Wang, C., Kang, J., Li, Y., Wang, M., 2014. Study on the mechanism of zonal disintegration around an excavation. *Int. J. Rock Mech. Min. Sci.* 67, 88–95. <https://doi.org/10.1016/j.ijrmms.2013.12.017>.
- Zuo, Y., Xu, T., Zhang, Y., Zhang, Y., Li, S., Zhao, G., Chen, C., 2012. Numerical study of zonal disintegration within a rock mass around a deep excavated tunnel. *Int. J. Geomech.* 12, 471–483. [https://doi.org/10.1061/\(ASCE\)GM.1943-5622.0000155](https://doi.org/10.1061/(ASCE)GM.1943-5622.0000155).